



TOR VERGATA
UNIVERSITÀ DEGLI STUDI DI ROMA

DOTTORATO DI RICERCA IN FISICA

CICLO DEL CORSO DI DOTTORATO XXXIII

**Search for the FCNC decay of top-quark in
c-quark and Z boson using the ATLAS detector**

LORENZO MARCOCCIA

A.A. 2020/2021

DOCENTE GUIDA: Prof. LUCIO CERRITO

COORDINATORE: Prof. ROBERTO BENZI

A dissertation submitted to the University of Rome Tor Vergata in accordance with the requirements of the degree of DOCTOR OF PHILOSOPHY in the Faculty of Physics.

32 NOVEMBER 2184

*'The wrong view of science
betrays itself in the craving to be right;
for it is not his possession of knowledge,
of irrefutable truth, that makes the man of science,
but his persistent and recklessly critical quest for truth.'*

(Karl Popper, The Logic of Scientific Discovery)

Ringraziamenti

Merci, merci, merci.

Abstract

Blablabla.

Contents

Introduction	1
1 The theory framework	3
1.1 The gauge principle in quantum field theory	4
1.1.1 Quantum Chromodynamics	5
1.1.2 The electro-weak sector	6
1.1.2.1 GIM mechanism	8
1.1.2.2 CKM matrix	9
1.2 Top quark physics	10
1.2.1 Production	10
1.2.2 Decay channels	11
1.3 Theories for physics beyond the Standard Model	12
1.3.1 Quark singlets	14
1.3.2 Two Higgs Doublet Model	15
1.3.3 Minimal Supersymmetric Standard Model	16
2 The LHC accelerator and the ATLAS experiment	18
2.1 The LHC accelerator	19
2.2 The ATLAS detector	22
2.2.1 Magnet System	24
2.2.2 Inner Detector	24
2.2.3 Calorimetric System	25
2.2.4 Muon Spectrometer	27
2.2.5 Trigger and Data Acquisition	29

3	The Trigger system upgrade for High-Luminosity LHC	30
3.1	ATLAS Barrel Muon Trigger	31
3.2	BI upgrade for Phase II	34
3.2.1	RPC upgrade	37
3.2.2	Trigger scheme	39
3.3	Hit digitization in the BI region	41
3.3.1	The cluster size model	41
3.3.2	Timing	46
3.4	L0 barrel trigger efficiency	48
3.4.1	BM and BO retrofitting	49
3.4.2	Dropping BIR and BIM chambers	52
4	Data modeling and object reconstruction	54
4.1	Event simulation	54
4.2	Object reconstruction	56
4.2.1	Electrons	56
4.2.2	Muons	57
4.2.3	Soft muons	58
4.2.4	Jets	59
4.2.5	Jet Flavour Tagging	59
4.2.5.1	Soft Muon Tagging	59
4.2.5.2	Recurrent Deep-Learning DL1r	59
4.2.6	Missing transverse momentum	60
4.2.7	Overlap removal	60
5	Search for the FCNC decay of top-quark in c-quark and Z boson	61
5.1	Physics motivation	62
5.2	Analysis strategy	65
5.3	Data and Monte Carlo samples	66
5.4	Event selections and reconstruction	67
5.4.1	Top quarks reconstruction	68
5.4.2	Signal Region definition	69
5.5	Background estimation	70
5.5.1	Control Regions definitions	71
5.5.2	Fake composition	72
5.6	Separation of signal from background events	73
5.6.1	GBDT discriminant definition	74
5.6.2	Input variables	75
5.6.3	GBDT training and evaluation	76
5.6.4	GBDT performance and over-training checks	77
5.7	Systematic uncertainties	78
5.7.1	Sources of systematic uncertainties	79
5.7.2	Acceptance and shape uncertainties	80

5.8	Additional Signal Regions and alternative c-tagger	81
6	Statistical analysis for tZc coupling	82
6.1	Strategy	82
6.2	Results	83
6.2.1	Background-only fit in CRs	84
6.2.2	Signal+Background fit in SR3	85
6.2.3	Signal+Background fit in SRs+CRs	86
7	Conclusions	87
A	Mass Resolution	88
References		89

Introduction

CONTENTS

CHAPTER 1

The theory framework

The construction of the Standard Model is the result of a long series of experiments and brilliant ideas in both theoretical and experimental fields. Towards the end of the 1960s, knowledge of what we consider to be the constituents elements of nature and the fundamental interactions among them, it was organized in the so-called Standard Model (MS), which aims to be a "theory of everything".

More recently, the only missing piece towards the completion of the SM, the Higgs boson, was discovered by the ATLAS and CMS collaborations.

The ambition is to find a theoretical representation of all phenomena experimentally accessible.

Since particle physics is characterized by phenomena that are both relativistic than quantum, the description of the Standard Model relies on the formalism of *Quantum Field Theories* (QFT), synthesis of quantum mechanical theory and relativistic. In these terms, the concept of field is associated both to material particles and to forces. Particles are mere manifestations of field: they are identified with the quanta of the material fields and force fields and the interaction among particles is determined by the exchange of virtual quanta of the field.

To search for extensions of the SM is possible postulate a scale of new physics high enough such that it will manifest itself through deviations of known observable, usually at high energies.

In this chapter, a concise description of the SM will be presented, from the gauge principle to the description of several theories for physics beyond the Standard Model which are crucial for the search of FCNC decay of top quark.

1.1 The gauge principle in quantum field theory

The mathematical framework of the SM is based on a quantum field theory description of the particles and their interactions. The interaction is a consequence of the invariance of physics under certain general symmetries: these invariances are called *gauge* because there is freedom in the choice of a certain number of parameters that can precisely "calibrate" the model. Each symmetry is therefore associated with a set of transformations that frame the "gauge group of the theory". The theory is introduced starting from the Lagrangian formalism developed in the classical mechanism, extending this formalism to classical field theory and finally to quantum field theory.

Lagrangian is defined as the difference between the kinetic energy and the potential energy of the system, as below:

$$\mathcal{L}(q, \dot{q}) = \frac{m}{2}(\dot{q})^2 - V(q) \quad (1.1)$$

and the *action* is defined as $S = \int dt \mathcal{L}(q, \dot{q})$.

Using a variational approach it can be shown that for any possible variation of the path of the particle, $\partial(q)$, the equation of motion of the system is the one that minimizes the *action*. The results are the so called *Euler-Lagrange* equations:

$$\frac{\mathcal{L}}{\partial q} - \frac{\partial}{\partial t} \frac{\mathcal{L}}{\partial \dot{q}} \quad (1.2)$$

The next step is the extension of the classical mechanics formalism to field theory. One possible way is to generalize the path of a particle which is a function of time $q(t)$, into a function of space-time coordinates $\phi(x)$ which is the vectorial (or tensorial) representation of the field with Lorentz invariance properties of the space-time.

The sub-set of dimension two vectorial representations used in particle physics is called spinors and they are divided into left-handed and right-handed, depending on their chirality: ψ_L and ψ_R . The usual representation for Lorentz and parity transformations is the *Dirac* spinor $\Psi = (\psi_L, \psi_R)$, which allows describing properly the dynamics of relativistic particles.

At this point, the Lorentz-invariant Lagrangian is the following:

$$\mathcal{L}_D = \bar{\Psi}(i\gamma^\mu \partial_\mu - m)\Psi \quad (1.3)$$

where γ are an extension of the Pauli matrices into a four dimension space-time and they are called Dirac matrices.

The QFT is also built on the *Noether's* theorem that relates symmetries of the system to conserved observables.

Through this theorem, symmetries become a fundamental building block of the physical theory. A particular set of transformations, called gauge transformations, which by construction leave invariant the Lagrangian of the SM, constitute a building principle of the SM itself.

Let us now consider the global $U(1)$ ¹ transformation of the form:

$$\Psi \rightarrow e^{i\theta}\Psi \quad (1.4)$$

It can be easily demonstrated that \mathcal{L}_D is invariant under such a transformation and the related conserved observable is the current $\bar{\Psi}\mu\Psi$.

However, the Lagrangian is no longer invariant under the transformation: $\theta \rightarrow \theta(x)$ which means that the gauge invariance is required in each point of the space-time.

The inclusion of an additional field, the photon, which mediates the forces, make the Lagrangian explicitly invariant and it allows to choose a *gauge* of the theory, in fact the action of free electromagnetic field is invariant under $A_\mu \rightarrow A_\mu - \partial\theta$, with A_μ being the four-vector of the electrostatic and magnetic potential: (V, \vec{A}) .

The above example is useful to understand how the SM is constructed. It is a gauge theory which, analogously to what described in this section, is invariant under:

$$SU(3)_c \otimes SU(2)_L \otimes U(1)_Y \quad (1.5)$$

The $SU(3)_c$ describes the strong force (see next section) while $SU(2)_L \otimes U(1)_Y$ term describes the electro-weak sector (see Section 1.1.2). A more detailed discussions follows.

1.1.1 Quantum Chromodynamics

The strong interaction between quark and gluons is described by the *Quantum Chromodynamics* (QCD). It is a gauge theory based on non-abelian $SU(3)_c$ ² and associated to the three colour charges (red, green and blue). A total number of 8 generators T^a of the group, also called Gell-Mann matrices, represent bosons mediating the force, called *gluons*. They are massless, in contrast with the weak mediators.

The QCD Lagrangian, can be expressed as:

$$\mathcal{L}_{QCD} = \bar{\psi}(i\gamma^\mu D_\mu - m)\psi - \frac{1}{4}G_{\mu\nu}^a G_a^{\mu\nu} \quad (1.6)$$

¹ $U(1)$ is the one-dimensional unitary group, i.e. any of its elements can be expressed as a 1×1 matrix whose inverse is equal to its transpose conjugate ($U^{-1} = \bar{U}^*$).

²S stands for "special", meaning that the group matrices have determinant 1. C stands for "colour", which is the conserved quantity associated with the symmetry

where the index a represent the 8 $SU(3)_C$ generators, $\frac{1}{4}G_{\mu\nu}^a G_a^{\mu\nu}$ is the kinetic term of the gluons (G^a is the gluon field strength tensor) and the covariant derivative D_μ is defined as

$$D_\mu = \partial_\mu - ig_s T_a G_\mu^a \quad (1.7)$$

The coupling constant α_s ($\frac{g_s^2}{4\pi} \sim 1$), is dependent from the transferred momentum Q^2 that correspond to a dependence from the separation between quarks:

$$\alpha_s(Q^2) = \frac{33 - 2n_f}{12\pi} \ln \left(\frac{Q^2}{\Lambda_{QCD}^2} \right) \quad (1.8)$$

where n_f is the number of quark flavours and Λ_{QCD}^2 is the QCD scale parameter, measured to be ~ 200 MeV that sets the scale between different regimes of the theory.

In fact one can discern two cases:

$$\alpha_s(Q^2) \xrightarrow[Q^2 \gg \Lambda_{QCD}^2]{} 0$$

$$\alpha_s(Q^2) \xrightarrow[Q^2 \ll \Lambda_{QCD}^2]{} \infty$$

In the first case, the quark coupling is asymptotically cancelled, in the limit $Q^2 \rightarrow \infty$, quarks can be considered as free particles and this phenomena calls *Asymptotic Freedom*. On the contrary, when the separation become relevant, the coupling is so strong to confine quarks in hadronic structures and this different phenomena calls *Confinement*. The only states that occur are completely antisymmetric in the colour variables (the colour singlets), which is equivalent to saying that the possible compositions of quarks must be "white".

Interaction between particles, that carry charges of colour, takes place through the exchange of gluons of the octet, therefore, not only between quarks and gluons but also between gluons and gluons. This is a very important difference between QED (*Quantum Electrodynamics*) and QCD. In QED, in fact, photons have no charge and cannot couple with each other.

1.1.2 The electro-weak sector

The first model of the weak interaction was proposed by Fermi in 1933, who proposed an effective field theory at low energies. According to this theory, charged current interactions are approximated by a point-like interaction with a coupling called G_F [1, 2]. At energies $\mathcal{O}(100 \text{ GeV})$ the theory breaks and the real propagator of the interaction is the W^\pm boson.

In 1957, a famous experiment conducted by Wu [3] proved that parity is maximally

violated by the charged weak interaction: it only couples to particles of left-handed chirality (and antiparticles of right-handed chirality). There also exists a neutral weak interaction, which couples both to left-handed and right-handed particles.

This discovery motivated the introduction of the vector-axial (V-A) structure of the Lagrangian of the weak force.

The model of the weak interaction was subsequently promoted to a gauge theory by requiring local invariance under symmetries of the $SU(2)$ group, and it was associated with a conserved quantity called the *weak isospin*.

Each generation of left-handed fermions forms a doublet satisfying $I_3 = \pm \frac{1}{2}$, while right-handed fermions correspond to singlets of null isospin, as follows:

$$\chi_L = \begin{pmatrix} \nu_l \\ l \end{pmatrix}_L \quad l_R \quad (1.9)$$

where $l = (e, \mu, \tau)$, and a right-handed neutrino singlet is not introduced since there is still no observation of such a particle. A similar representation is given for quarks where both up (u, s, t) and down-types (d, c, b) have a right-handed component, singlet under $SU(2)_L$.

The transitions between quark doublet members corresponds to $SU(2)$ raising (τ^+) and lowering (τ^-) operators, giving the charge raising and lowering currents [4]:

$$\begin{aligned} J^+ &\sim g(\bar{u} d_c) = g(\bar{u} \bar{d}_c) \begin{pmatrix} 0 & 1 \\ 0 & 0 \end{pmatrix} \begin{pmatrix} u \\ d_c \end{pmatrix} = g(\bar{q} \tau^+ q) \\ J^- &\sim g(\bar{d}_c u) = g(\bar{u} \bar{d}_c) \begin{pmatrix} 0 & 0 \\ 1 & 0 \end{pmatrix} \begin{pmatrix} u \\ d_c \end{pmatrix} = g(\bar{q} \tau^- q) \end{aligned} \quad (1.10)$$

where overall numerical factors have been omitted, d-quark is 'Cabibbo-rotated' ($\theta_c \sim 13^\circ$) and g is the dimensionless weak coupling constant and quarks.

If there exist an appropriate symmetry, based on some underlying gauge theory, then a current involving τ_3 is also expected, since these operators are related via the commutation relation $[\tau^+, \tau^-,] = 2\tau_3$. Hence, with such a gauge theory symmetry, one would expect the existence of a neutral current (identified by the Z^0 boson) of the form :

$$\begin{aligned} J^0 &\sim 2g(\bar{q} \tau_3 q) = g(\bar{u}u - \bar{d}_c d_c) \\ &= g[\bar{u}u - \bar{d}_c d \cos^2 \theta_c - \bar{s}_c s \sin^2 \theta_c - (\bar{d}s + \bar{s}d) \cos \theta_c \sin \theta_c] \end{aligned} \quad (1.11)$$

The terms $\bar{d}s$ and $\bar{s}d$ correspond to strangeness-changing neutral currents (SCNC), which are heavily suppressed in nature.

For example, the decay branching ratio $K^+ \rightarrow \mu^+ \nu_\mu$ is 63.5%, whereas that for $K_L^0 \rightarrow \mu^+ \mu^-$ is $\sim 10^{-8}$.

A mechanism to suppress this unwanted strangeness-changing neutral currents was suggested in 1970 by Glashow, Iliopoulos and Maiani (GIM) and it will be described in the next section.

1.1.2.1 GIM mechanism

Until the beginning of the 1970s, the only three light quarks u, d and s known at this time could explain the observed hadron spectrum and the observed weak decays of pions and kaons were mostly in good agreement with the predictions of the *Cabibbo mechanism*. Glashow, Iliopoulos and Maiani proposed the existence of a second orthogonal doublet, additional to $(\begin{smallmatrix} u \\ d_c \end{smallmatrix})$, containing a new quark c (charm) with charge $\frac{2}{3}$, as follows [5]:

$$q' = \begin{pmatrix} c \\ s_c \end{pmatrix} = \begin{pmatrix} c \\ -d \sin \theta_c + s \cos \theta_c \end{pmatrix} \quad (1.12)$$

Adding this term gives the total neutral current:

$$\begin{aligned} J^0 &\sim 2g(\bar{q} \tau_3 q + \bar{q}' \tau_3 q') = g(\bar{u}u + \bar{c}c - \bar{d}_c d_c - \bar{s}_c s_c) \\ &= g[\bar{u}u + \bar{c}c - \bar{d}d - \bar{s}s] \end{aligned} \quad (1.13)$$

That is, the unwanted terms cancel, leaving a flavour diagonal result.

The GIM mechanism gives also an estimation of the charmed quark, before the J/Ψ discovery occurred in 1974.

In the three-quarks picture, and according to the Cabibbo mechanism alone, $s \rightarrow d$ transitions via *Flavour Changing Neutral Current* FCNC processes would be possible at all orders of the perturbation expansion.

For example, the process $K_L^0 \rightarrow \mu^+ \mu^-$ FCNC decay could take place, in terms of known quark (u and d-quarks), via the "box-diagram" of Figure 1.1(a).

The calculated rate is larger than what was observed experimentally.

However, including the diagram of Figure 1.1(b), the total amplitude is:

$$\mathcal{M} = \mathcal{M}_{(a)} + \mathcal{M}_{(b)} \sim f(m_u)g^4 \cos \theta_c \sin \theta_c - f(m_c)g^4 \cos \theta_c \sin \theta_c \quad (1.14)$$

Thus, the c-quark induces a cancellation, giving a BR compatible with the experiments, but not a total cancellation because $m_c \neq m_u$. Hence, the predictions on the mass of the c-quark that in the end it is ~ 3 GeV. In addition to this major prediction, the GIM mechanism led to the prediction that FCNC processes are forbidden at tree-level Leading Order. The branching ratios of several FCNC decays of the top quark in the SM are given in Table 1.1. The FCNC production is also sensitive to numerous new physics models, as is mentioned in more details in Section 1.3.

The GIM hypothesis represent a generalization of Cabibbo's idea. The introduction of the fourth quark (c) restored the symmetry in the (then known) numbers of quark and

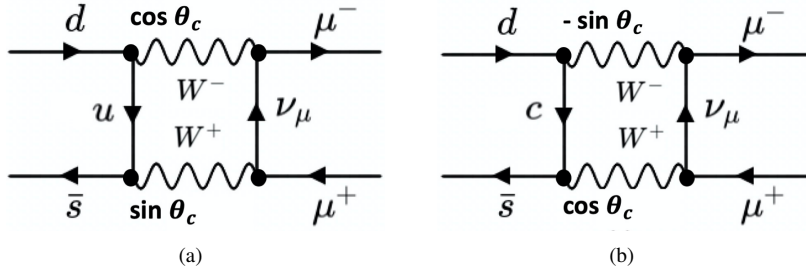


Figure 1.1 – Feynman diagrams of $K_L^0 \rightarrow \mu^+ \mu^-$ via (a) u-quark exchange and (b) c-quark exchange

	$t \rightarrow uZ$	$t \rightarrow cZ$	$t \rightarrow u\gamma$	$t \rightarrow c\gamma$	$t \rightarrow ug$	$t \rightarrow cg$	$t \rightarrow uH$	$t \rightarrow cH$
BR	8×10^{-17}	1×10^{-14}	3.7×10^{-16}	4.6×10^{-14}	3.7×10^{-14}	4.6×10^{-12}	2×10^{-17}	3×10^{-15}

Table 1.1 – Branching ratios for top quark FCNC interactions in the SM [6].

leptons.

These ideas were extended by Kobayashi and Maskawa (1973), who introduced a framework of six quarks and it will be described in the next section.

1.1.2.2 CKM matrix

In 1973 Kobayashi and Maskawa extended the Cabibbo's mechanism allowing to describe the transitions within and in-between 3 generations of quarks using the so-called *CKM* 3×3 matrix [7, 8], which relates the weak eigenstate of down-type to their mass eigenstate:

$$\begin{pmatrix} d' \\ s' \\ b' \end{pmatrix} = V_{CKM} \begin{pmatrix} d \\ s \\ b \end{pmatrix} = \begin{pmatrix} |V_{ud}| & |V_{us}| & |V_{ub}| \\ |V_{cd}| & |V_{cs}| & |V_{cb}| \\ |V_{td}| & |V_{ts}| & |V_{tb}| \end{pmatrix} \begin{pmatrix} d \\ s \\ b \end{pmatrix} \quad (1.15)$$

By convention, the up-type quarks are taken to be pure states. Therefore, partners of the up-type quarks within the weak isospin doublets are the weak eigenstates d' , s' and b' which are the pure states.

The CKM matrix is fully defined by 4 independent parameters, which must be determined experimentally. These parameters are: 3 mixing angles and 1 CP-mixing phase, which violates the CP³ symmetry in the SM [9]. The diagonal elements of the CKM matrix are close to 1, reflecting the fact that transitions are favoured between quarks of the same generation. The CKM matrix is unitary, i.e. the sum of the transition probabilities for any quark flavour is equal to 1. If this assumption was to be disproved, it could imply the existence of a fourth quark generation.

³Charge transformation followed by a parity transformation.

1.2 Top quark physics

The heaviest known elementary particle described by the Standard Model is the top quark.

In 1995, the top quark discovery in FERMILAB [10, 11] was a great success for the SM predictions e.g. the corroboration of existence of a weak isospin partner of the top quark. Due to its large mass, the predicted lifetime $\tau_t \approx 5 \times 10^{-25}$ s (in agreement with theoretical expectations [12]) entail that it decays before hadronising.

In the next sections, the production mechanism is reported, as well as a dissertation about the decay channels.

1.2.1 Production

The top quark can either be produced as pairs, via strong interaction, or as a single top quark via electroweak interaction that does not preserve the flavour.

The main parton sub-processes that lead to top-pair production are the quark-antiquark annihilation ($q\bar{q} \rightarrow t\bar{t}$, Figure 1.2(a)) and the gluon-gluon fusion ($gg \rightarrow t\bar{t}$, Figures 1.2(b) and 1.2(c)).

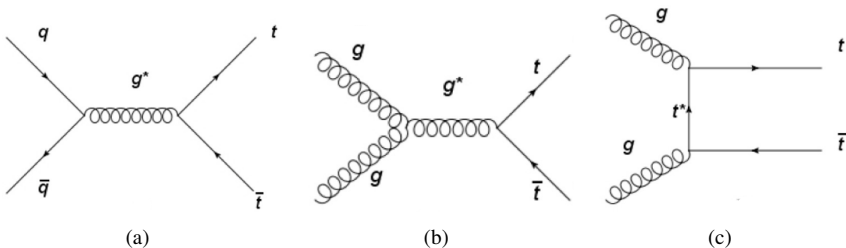


Figure 1.2 – Feynman diagrams of $t\bar{t}$ production via (a) quark-antiquark annihilation ($q\bar{q} \rightarrow t\bar{t}$) and (b,c) gluon-gluon fusion ($gg \rightarrow t\bar{t}$)

Since in protons there are not valence antiquarks, the quark-antiquark annihilation is suppressed by the parton distribution functions (PDF) of the antiquark in the proton. Therefore, at LHC the dominant process turns out to be the gluon-gluon fusion, while in a proton-antiproton collider, such as Tevatron, the dominant process is the quark-antiquark annihilation, in fact:

- Tevatron: $q\bar{q} \rightarrow t\bar{t} \approx 86\%$, $gg \rightarrow t\bar{t} \approx 15\%$
- LHC: $q\bar{q} \rightarrow t\bar{t} \approx 20\%$, $gg \rightarrow t\bar{t} \approx 80\%$

Top-pairs can be produced also for weak interaction when two quarks exchange Z^0 or a γ ; however the cross-section of these type of processes is negligible when compared to

the production cross-section through strong interaction.

Although at LHC the top quarks are mainly produced in the process described above, a not negligible number of tops are produced singly by weak interaction but with a production cross section equal to approximately 1/3 of the top-pair production cross-section, which is, at $\sqrt{13}$ TeV and taking into account a top quark mass of $172.5 \text{ GeV}/c^2$, $\sigma_{t\bar{t}} = 831.8^{+19.8+35.1}_{-29.2-35.1} \text{ pb}$ [13].

1.2.2 Decay channels

Since the top quark mass is higher than the W boson mass, it decays through weak interaction, mainly in $t \rightarrow W^+ b$; according to SM is 100% of the possible cases.

The other channels ($t \rightarrow W^+ s$, $t \rightarrow W^+ d$) are strongly suppressed by the CKM matrix elements (see Section 1.1.2.2). Exploiting the matrix unitarity and the B meson oscillations it is possible to extract the following BRs[14]:

$$\begin{aligned}\text{BR}(t \rightarrow W^+ b) &\sim 0.998 \\ \text{BR}(t \rightarrow W^+ s) &\sim 1.9 \cdot 10^{-3} \\ \text{BR}(t \rightarrow W^+ d) &\sim 10^{-4}\end{aligned}$$

Therefore, the top decay total width is given by, in good approximation, the decay ($t \rightarrow W^+ b$), thus equals to $\Gamma_t = 1.44 \text{ GeV}$. The W boson may decay in only two ways: "leptonically" ($W \rightarrow l\nu$) or "hadronically" ($W \rightarrow q\bar{q}'$). This leads to three different categories of $t\bar{t}$ decays: dileptonic, semi-leptonic or hadronic.

Figure 1.3 summarize the BRs associated to each channel.

At the hadron colliders, the dominant hadronic mode is the hardest to detect due to the large QCD background.

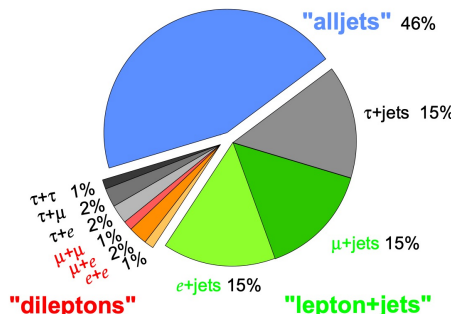


Figure 1.3 – Branching ratios associated to each $t\bar{t}$ decay channel[15].

1.3 Theories for physics beyond the Standard Model

The previous sections describe the core components of what we call *Standard Model* and report few major successes of many. Its predictive power makes this model the most tested in physics and it reaches the culmination of success on 4 July 2012, when the ATLAS and CMS experiments at CERN announced the observation a new particle in the mass region around 125 GeV, the Higgs boson [16].

But in spite of its important achievements, the SM falls short of explaining several important observations that in this section are briefly reported.

SM considers neutrinos as massless particles but this is in contradiction with the results of many experiments, which observed, in several different contexts, the *neutrino oscillations*.

It is a quantum mechanical phenomenon whereby a neutrino created with a specific lepton family number (e , μ , or τ) can later be measured to have a different lepton family number and this mechanism, implies that the neutrino has a non-zero mass since it arises from mixing between the flavour and mass eigenstates of neutrinos.

SM can not describe *dark matter* and *dark energy*. The first evidence of dark matter came with the observation of the rotational speed of galaxies, which suggests the existence of a huge amount of undetected mass [17].

None of the SM particles could explain this phenomenon and, since a dark matter has never been directly observed implies that it interact only weakly with the ordinary matter and radiation or does not interact at all.

Likewise, dark energy is an unknown form of energy that affects the universe on the largest scales. The first observational evidence for its existence came from supernovae measurements, which showed that the universe does not expand at a constant rate; rather, the expansion of the universe is accelerating.

The data collected by Planck spacecraft, indicate that dark energy contributes 68% of the total energy in the present-day observable universe. The mass–energy of dark matter and ordinary (baryonic) matter contributes 27% and 5%, respectively, and other components such as neutrinos and photons contribute a very small amount [18].

After the Big Bang one could expect that the universe produced the same amount of particles-antiparticles and that the constant annihilation of pairs would have constituted a universe of radiation. What we observe actually is large cosmological matter (but not antimatter) structures. The mechanism suggested by the SM through the CP-symmetry violation of neutral oscillating hadrons is not sufficient to explain alone this phenomenon.

There are also some other strong indications that the SM could be not yet complete. Indeed, it is based on 19 parameters (excluding neutrino masses) that must be deter-

mined experimentally and no known theoretical origin. Moreover, gravity could not be included as a gauge theory because, describing graviton (the associated gauge boson) interactions, the classical theory of Feynman diagrams, and semiclassical corrections with at least two loops lead to *ultraviolet divergences*. These infinite results cannot be removed because quantized general relativity is not perturbatively renormalizable, unlike QED and models such as the Yang–Mills theory. Therefore, when the probability of a particle to emit or absorb gravitons is calculated, the theory loses predictive veracity. Those problems and the complementary approximation framework are grounds to show that a theory more unified than quantized general relativity is required to describe the behaviour near the Planck scale.

The problem of *naturalness* is also much debated in literature. The Higgs boson is very sensitive to loop corrections (involving top quark and himself mainly) and if one considers the a theory close to the Planck scale, thus these corrections may explain why the Higgs boson mass is so relatively small compared e.g. with the top quark mass. Another problem is, in fact, the mass scale of fermions that it ranges across many orders of magnitude without any clear explanation.

Many are models of "new physics" that attempt to describe and explain the phenomena mentioned above but so far there is no evidence of new physics Beyond Standard Model (BSM). In the SM, top quark decays almost exclusively into bW while flavour-changing neutral current (FCNC) decays such as $t \rightarrow qZ$ are forbidden at tree level. FCNC decays occur at one-loop level (Figure 1.4) but are strongly suppressed by the GIM mechanism (Section 1.1.2.1), with a suppression factor of 14 orders of magnitude relative to the dominant decay mode[19].

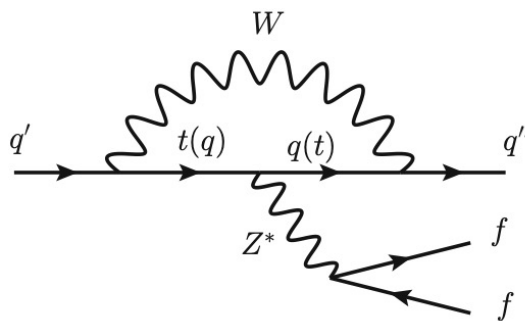


Figure 1.4 – Sketched Feynman diagram for SM $q' \rightarrow q'' f \bar{f}$ induced by the tqZ coupling, where q' and q'' denote the down-type quarks; $q = u, c$, and f can be any possible fermions. In the Standard Model, FCNC processes are forbidden at tree level but occur at one-loop level (see GIM mechanism in Section 1.1.2.1).

However, in the BSM models, the suppression could be relaxed and the loop diagrams mediated by new bosons that could contribute, leading to couplings of many orders of magnitude higher than those expected by the SM.

Examples of such extensions are the quark-singlet model (QS)[20], the two-Higgs-doublet model with (FC 2HDM) or without (2HDM) flavour conservation[21], the Minimal Supersymmetric Standard Model (MSSM)[22], the MSSM with R-parity violation (RPV SUSY)[23], models with warped extra dimensions (RS)[24], or extended mirror fermion models (EMF) [25]. Reference [26] gives a comprehensive review of the various extensions of the SM that have been proposed. Table 1.2 provides the maximum values for the branching ratios predicted by these models and compares them to the value predicted by the SM.

In this section we will briefly describe some of these theories interesting for the topics of this thesis.

Model:	SM	QS	2HDM	FC 2HDM	MSSM	RPV SUSY	RS	EMF
$\mathcal{B}(t \rightarrow qZ)$	10^{-14}	10^{-4}	10^{-6}	10^{-10}	10^{-7}	10^{-6}	10^{-5}	10^{-6}

Table 1.2 – Maximum allowed FCNC $t \rightarrow qZ$, ($q = u, c$) branching ratios predicted by several models[19–26].

1.3.1 Quark singlets

The need to suppress the FCNC mechanism lead to two dogmas [27, 28]:

- they are not mediated by Z^0 boson at tree-level
- no FCNC mechanism in the scalar sector at tree-level

It is possible to overcome these dogmas using extensions of the SM, like the Quark Singlets (QS) [29] that introduces a vector-like quark ($Q = \frac{1}{3}$ or $Q = \frac{2}{3}$), thus a small violation of the $3 \times 3 V_{CKM}$ unitarity (see Section 1.1.2.2), mediated by Z^0 boson and natural FCNC suppression at tree-level.

Given x_L and x_R , $SU(2)_L$ singlets

$$\begin{pmatrix} d' \\ s' \\ b' \\ x' \end{pmatrix} = \begin{pmatrix} |V_{ud}| & |V_{us}| & |V_{ub}| & |V_{ux}| \\ |V_{cd}| & |V_{cs}| & |V_{cb}| & |V_{cx}| \\ |V_{td}| & |V_{ts}| & |V_{tb}| & |V_{tx}| \end{pmatrix} \begin{pmatrix} d \\ s \\ b \\ x \end{pmatrix} \quad (1.16)$$

The non orthogonality of the columns leads to terms of the type:

$$J_\mu = \frac{g}{\cos\theta_W} Z_{bd} \bar{b}_L \gamma_\mu d_L Z^\mu \quad (1.17)$$

where

$$Z_{bd} = V_{ud}V_{ub}^* + V_{cd}V_{cb}^* + V_{td}V_{tb}^* \quad (1.18)$$

and Z_{bd} is suppressed by $\frac{m_q}{m_x}$.

In this way it is possible to have deviations from 3×3 unitarity.

The PMNS matrix in the leptonic sector, in the context of see-saw mechanism is not 3×3 unitarity [30].

Vector-like quarks provide the simplest model with spontaneous *CP violation* and a framework to have a common origin of all CP violation because it is a potential solution of the *strong CP problem* without involving other particles, e.g. axions.

1.3.2 Two Higgs Doublet Model

The LHC discovery of a Standard-Model-like Higgs $H(125)$ particle in 2012[16] could be a portal to an extended Higgs sector predicted by several models, one of this is the Two-Higgs-Doublet Model (2HDM) [31]. The most natural extension of the Standard Model scalar sector is the addition of an extra $SU(2)_L$ doublet.

The 2HDM is an *Effective Field Theory* (EFT⁴) consisting of two complex Higgs doublets, which provide masses to both the up-type and the down-type fermions:

$$\Phi_1 = \begin{pmatrix} \phi_1^+ \\ \phi_1^0 \end{pmatrix} \quad \Phi_2 = \begin{pmatrix} \phi_2^+ \\ \phi_2^0 \end{pmatrix} \quad (1.19)$$

with the minimum of the potential corresponding to

$$\Phi_{1,0} = \frac{1}{\sqrt{2}} \begin{pmatrix} 0 \\ \nu_1 \end{pmatrix} \quad \Phi_{2,0} = \frac{1}{\sqrt{2}} \begin{pmatrix} 0 \\ \nu_2 \end{pmatrix}. \quad (1.20)$$

After the electroweak symmetry breaking (EWSB), there are five physical scalar fields, consisting of neutral bosons h, H, A of which the first two bosons are CP-even, opposed to the A -boson which is CP-odd and of two charged Higgs states H^\pm .

The model is parametrized by the five Higgs masses (m_H, m_h, m_{H^\pm}, m_A), the ratio of the vacuum expectation values of the two Higgs doublets $\tan \beta = \nu_2/\nu_1$ and the mixing angle α between the CP-even Higgs states.

There exist four types of 2HDM which simultaneously forbid the presence of FCNC and preserve CP symmetry:

- in Type I all fermions couple to the second doublet Φ_2 . It follows that BR are independent of $\tan \beta$;

⁴An EFT corresponds to a low-energy approximation to a more fundamental underlying theory, characterized by an energy scale Λ (e.g. the mass of new particles)

- in Type II or MSSM-like scenario, lepton and down-type quarks couple to the first doublet Φ_1 , whilst up-type quarks couple to Φ_2 ;
- in Type III or lepton specific scenario, quarks couple to Φ_2 while leptons couple to the other doublet;
- in Type IV or flipped model, the coupling of the leptons is reversed with respect to the Type-II model.

1.3.3 Minimal Supersymmetric Standard Model

The FCNC processes have also been studied with the *Minimal Supersymmetric Standard Model* (MSSM), where loop corrections of the supersymmetric QCD with gluinos and scalar quarks, as shown in Figure 1.5. In supersymmetric QCD it was shown that there

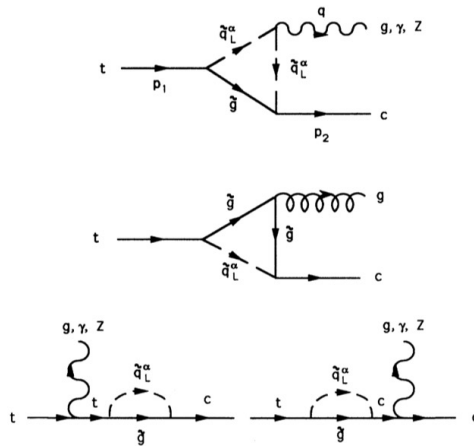


Figure 1.5 – The diagrams with scalar quarks and gluinos within the loop, which contribute to the top quark decay into a charm quark and a Z boson, photon, or gluon[32].

occur flavour-changing strong interactions between the gluino, the left-handed quarks, and their supersymmetric scalar partners, whereas the couplings of the gluino to the right-handed quarks and their partners remains flavour diagonal. To calculate the one-loop diagrams shown in Figure 1.5 we need the couplings of the gluon to the gluinos, of the scalar partners of the left-handed quarks to the gluon, photon, and Z boson, and of the gluino to the left-handed quark and its scalar partner.

After the introduction of non-trivial squark mixing, is possible to calculate the coupling that leads to flavour changing in which appears K_{ij} , the supersymmetric version of

V_{CKM} :

$$\begin{pmatrix} 1 & \epsilon & \epsilon^2 \\ -\epsilon & 1 & \epsilon \\ -\epsilon^2 & -\epsilon & 1 \end{pmatrix} \quad (1.21)$$

It is possible to demonstrate that all divergent terms cancel exactly, without the GIM mechanism.

Finally, we define $\mathcal{B}(t \rightarrow cZ) = \frac{\Gamma_S(t \rightarrow cZ)}{\Gamma_W(t \rightarrow bW)}$, where:

$$\Gamma_W(t \rightarrow bW) = \frac{\alpha}{16 \sin \Theta_W} m_{top} \left(1 - \frac{m_W^2}{m_{top}^2} \right)^2 \left(2 + \frac{m_{top}^2}{m_W^2} \right) \quad (1.22)$$

Using the following values for the parameters $m_{top} = 174$ GeV, $\alpha_s = 1.4675 / \ln \left(\frac{m_{top}^2}{\Lambda_{QCD}^2} \right)$ with $\Lambda_{QCD} = 0.18$ GeV, is possible to see the branching ratio $\mathcal{B}(t \rightarrow cZ)$ as a function of the scalar mass m_S for a gluino mass of 100 GeV (Figure 1.6).

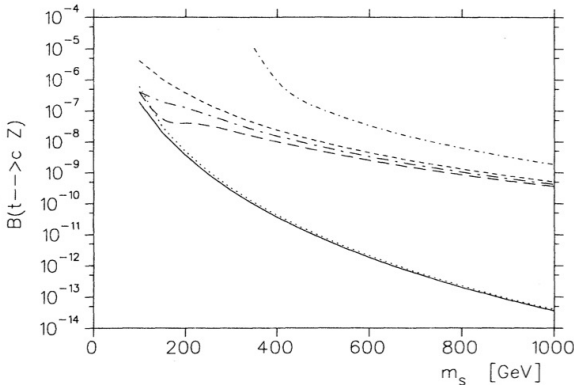


Figure 1.6 – The branching ratio $\mathcal{B}(t \rightarrow cZ)$ as a function of the scalar mass m_S . The gluino mass was taken to be 100 GeV. The solid line is the unphysical case with no squark mixing, the dotted lines are different scenarios of squark mixing[32].

We see that without mixing, $\mathcal{B}(t \rightarrow cZ)$ decreases rapidly with increasing scalar mass. The mixing has a drastic effect. It enhances the branching ratio by up to 5 orders of magnitude for large m_S .

CHAPTER 2

The LHC accelerator and the ATLAS experiment



Figure 2.1 – The LHC ring, aerial view.

This chapter main focus is the experimental setup, thus the ATLAS detector, one of the four large experiments at CERN (*Conseil Européen pour la Recherche Nucléaire*) and shown in Figure 2.1.

Established in 1954, CERN is the largest particle physics laboratory in the world and the organization is based in a north-west suburb of Geneva on the Franco-Swiss border. The analysis presented in this thesis is based on the data collected in the 2015, 2016, 2017 and 2018. Since December 2018, LHC has been shut-down (LS2, 2019-2020) to undergo a major upgrade (Phase I Upgrade) which may enable to collect up to 300 fb^{-1} at a c.o.m. energy of 14 TeV until 2023. After that, a second major upgrade (Phase II Upgrade) is planned to the LHC (LS3, 2014-2025) which will increase the interaction rate by a factor of 10; this upgrade will lead LHC to High-Luminosity LHC (HL-LHC).

2.1 The LHC accelerator

Located at CERN, the Large Hadron Collider (LHC) [33]. is the world's highest energy particle accelerator. LHC is a circular hadron accelerator, positioned at a depth of about 100 m in the tunnel built for the LEP accelerator, at CERN in Geneva. It is 26.6 km long and currently operates by making proton beams collide at an energy $\sqrt{s} = 13$ TeV.

CERN's choice to replace the LEP leptonic collider with an hadronic one, such as LHC, has brought two fundamental advantages: the first is that for the same infrastructural size it is possible to reach a higher energy in the center of mass, since the energy lost by radiation of synchrotron from a particle in circular motion is $\frac{dE}{dt} \propto \frac{E^4}{m^4 R}$, where R is the bending radius and m is the mass of the accelerated particle travelling at an energy E . The second advantage is that the composite structure of the protons allows access to a wider energy spectrum that can be explored simultaneously without having to change the beam parameters. On the other hand, the number of events considered as a background also increases. In addition to proton-proton (p-p) collisions, at LHC collisions between heavy lead ions (Pb-Pb) also occur .

Before reaching the highest possible energy at the LHC, the protons undergo subsequent acceleration steps. The overall accelerator complex is shown in Figure 2.2.

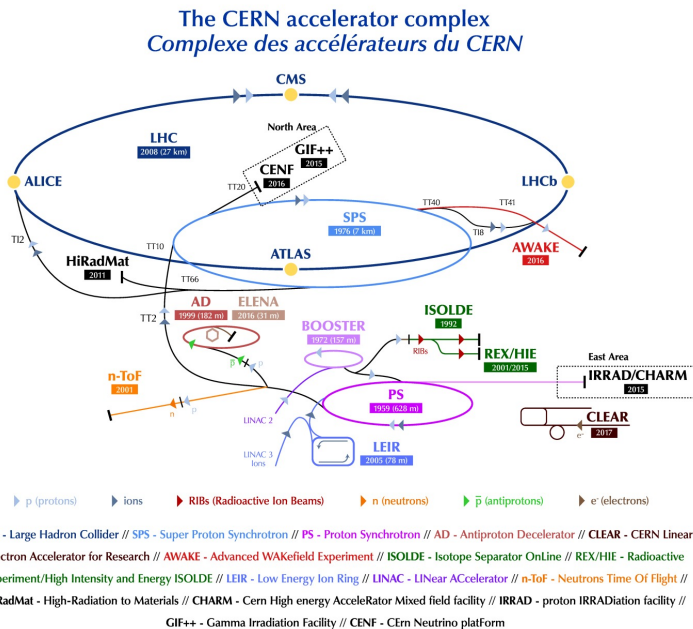


Figure 2.2 – The overall CERN accelerator complex [34].

The first step is the proton production from hydrogen gas and they are accelerated up to 50 MeV at the LINear ACcelerator 2 (LINAC 2). These protons are then injected into the Proton Synchrotron Booster (PSB) where their energy reach 1.8 GeV. The acceleration chain continues into the Proton Synchrotron (PS) which pushes the beam to 25 GeV. After that, the beam is injected into the Super Proton Synchrotron (SPS) where the protons are accelerated up to 450 GeV. Finally, the bunches of protons are injected in the LHC. A typical bunch train corresponds to 2808 bunches for each beam with 25 ns separation and a bunch contains about 10^{11} protons) colliding at a rate up to 40 MHz. The LHC is designed to accelerate each beam at an energy of 7 TeV thanks to a complex system of dipole and higher order magnets but the LHC performance has not always been those observed to the present day.

The first protons beams circulated in the LHC for the first time in September 10th of 2008. From 2010 to 2012, the protons beams had an energy of 3.5 TeV. From 2012 to 2013, the energy reached was 4 TeV per beam. The first shutdown ended when the LHC started to accelerate beams up to an energy of 6.5 TeV in April 5th of 2015.

Since protons are charged particles, a strong magnetic field, produced by 1232 superconducting electromagnets, curve the beams around the circular accelerator. To maintain the superconductivity properties, these magnets requires a temperature of 1.9 K ($\approx 271.3^{\circ}\text{C}$). This temperature allows this dipole magnets to generate a magnetic field of 8 T. Besides this magnets, a total of 392 quadrupole magnets maintain the beams focused and 16 radio-frequency cavities accelerate particles and keep them in controlled bunches with a constant energy. Four main interaction points are used as collisions points corresponding to the location of the four detectors: ALICE, ATLAS, CMS and LHCb.

The beam in the LHC is not continuous but rather divided in a collection of protons (bunches) colliding at a rate up to 40 MHz. The LHC beam at full intensity nominally consists of 2808 bunches and each bunch contains $\approx 1.15 \times 10^{11}$ protons, spaced by 25 ns.

The number of multiple interactions per bunch crossing is called *pile-up* and it is denoted by μ . Actually there are two different sources of pile-up:

- in-time pile-up occurs when multiple collisions take place in a single bunch crossing
- out-of-time pile-up is due to finite read-out time resolution of the detectors, often larger than 25 ns. In this case, the residual energy from a previous bunch crossing could potentially be associated to the following bunch crossing.

The distribution of $\langle \mu \rangle$ is shown in Figure 2.3, for the different data-taking periods. The average pile-up for 2015-2018 is $\langle \mu \rangle = 33.7$.

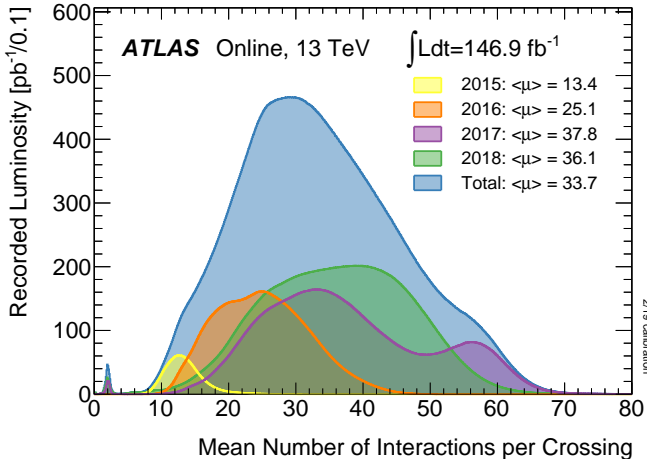


Figure 2.3 – Luminosity-weighted distribution of the mean number of interactions per crossing for the 2015-2018 pp collision data at $\sqrt{13}$. All data recorded by ATLAS during stable beams is shown, and the integrated luminosity and the mean μ value are given in the figure [35].

The event rate of a given process with cross section σ is given by $\frac{dN}{dt} = \mathcal{L}\sigma$, where \mathcal{L} is a characteristic of the accelerator, known as *instantaneous luminosity* and is given by:

$$\mathcal{L} = \frac{N_b^2 k_b f \gamma}{4\pi \sigma_x \sigma_y} F \quad (2.1)$$

where N_b^2 is the number of particles per bunch, k_b is the number of bunches, γ represents the relativistic gamma factor, f is the revolution frequency of the accelerator, σ_x and σ_y are the horizontal and vertical beam size, F is a geometrical correction factor from the crossing-angle of the two beams at the interaction point (IP).

Given a period of time T , one can define the *integrated luminosity* as $L = \int_0^T dt \mathcal{L}$ which is typically expressed in fb^{-1} (1 b = 10^{-28}m^{-2}).

Figure 2.4 shows the total integrated luminosity over the full LHC data taking period at $\sqrt{13}$ TeV and Table 2.1 summarize the main design parameters of LHC.

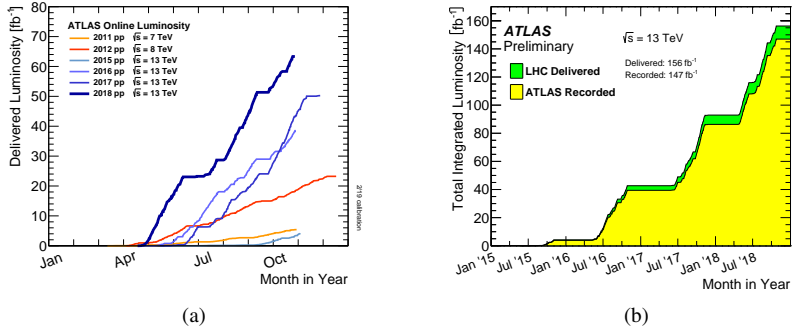


Figure 2.4 – Cumulative luminosity versus (a) day delivered to ATLAS during stable beams; (b) time delivered to ATLAS (green) and recorded by ATLAS (yellow) during stable beams for pp collisions at $\sqrt{13}$ [35].

Parameter	2015	2016	2017	2018
Bunch intensity [$\times 10^{11}$ p]	1.2	1.1	1.25	1.15
Number of bunches	2200	2200	1900	2500
Emittance [μm]	3.5	2.5	2.0	2.2
Crossing angle [μrad]	290	280	300	300
Peak luminosity [$10^{34}\text{cm}^2\text{s}^{-1}$]	0.5	1.5	1.5	2.0

Table 2.1 – Main beam parameters of proton-proton collisions of LHC in Run2.

2.2 The ATLAS detector

ATLAS (A Toroidal LHC ApparatuS) [36] is a multi-purpose apparatus whose primary goal is to identify and measure the properties of particles produced in p-p collision. The overall ATLAS detector layout is shown in Figure 2.5.

The ATLAS detector consist of a concentric cylinder shape (4π coverage), therefore nominally forward-backward symmetric with respect to the interaction point (IP) where the proton beams collide in it. It can be divided into five main parts:

- Magnet System (section 2.2.1);
- The Inner Detector (section 2.2.2);
- The Calorimetric System (section 2.2.3);
- Muon Spectrometer (section 2.2.4).
- Trigger and data acquisition System (section 2.2.5).

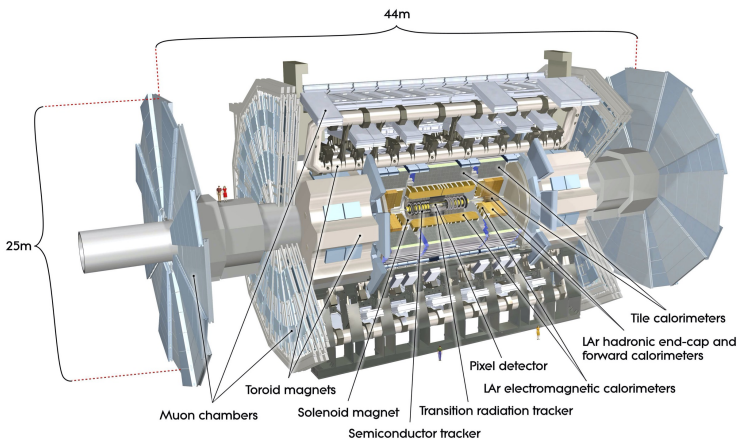


Figure 2.5 – Cut-away view of the ATLAS detector. The dimensions of the detector are 25 m in height and 44 m in length. The overall weight of the detector is approximately 7000 tonnes [36].

Coordinate system

The ATLAS coordinate system is a right-handed Cartesian coordinate system with the origin defined at the IP, in the center of the detector.

The z -axis corresponds to the beam pipe while the x and y directions define the transverse plane.

A cylindrical coordinate system is often used due to the geometry of the detector, where ϕ is the azimuthal angle and θ is the polar angle. ϕ is orthogonal to the beam direction, therefore it is invariant under a Lorentz boost(z -axis), while θ is not an invariant, so the *pseudorapidity* is defined as:

$$\eta = -\ln \left(\tan \left(\frac{\theta}{2} \right) \right) \quad (2.2)$$

Pseudorapidity is an approximation of the *rapidity*¹ for relativist particles ($m \ll p$). The distance between two objects is indicated using ΔR , defined as:

$$\Delta R = \sqrt{\Delta\eta^2 + \Delta\phi^2} \quad (2.3)$$

The transverse momentum is the projection of the momentum orthogonal to the beam direction is defined as:

$$p_T = \sqrt{p_x^2 + p_y^2} \quad (2.4)$$

¹Rapidity is defined as $y = \frac{1}{2} \ln \frac{E+p_z}{E-p_z}$

2.2.1 Magnet System

The magnet configuration comprises a thin superconducting solenoid surrounding the inner-detector cavity, and three large superconducting toroids (one barrel and two end-caps) arranged with an eight-fold azimuthal symmetry around the calorimeters. This fundamental choice has driven the design of the rest of the detector.

The inner detector is immersed in a 2 T solenoidal field provided by the central solenoid with inner radius of 1.23 m and a total length of 5.8 m.

It is designed to minimize the amount of material in front of the calorimeter to have a small impact on the energy measurement. This is achieved by hosting the solenoid and the cryostat in the same vacuum vessel of the electromagnetic calorimeter.

The overall dimensions of the magnet system is 26 m long and 20 m diameter and provide and average magnetic field intensity of 0.5 T in the barrel and 1 T in the end-caps regions [37].

2.2.2 Inner Detector

The Inner Detector (ID) [36] is the detector system closest to the beam.

It is composed of three detectors: the semiconductor pixel detector (PIXEL), the microstrip detector SCT (Semi-Conductor Tracker), and the most external, the transition radiation detector TRT (Transition Radiation Tracker).

Its overall layout is depicted in Figure 2.6.

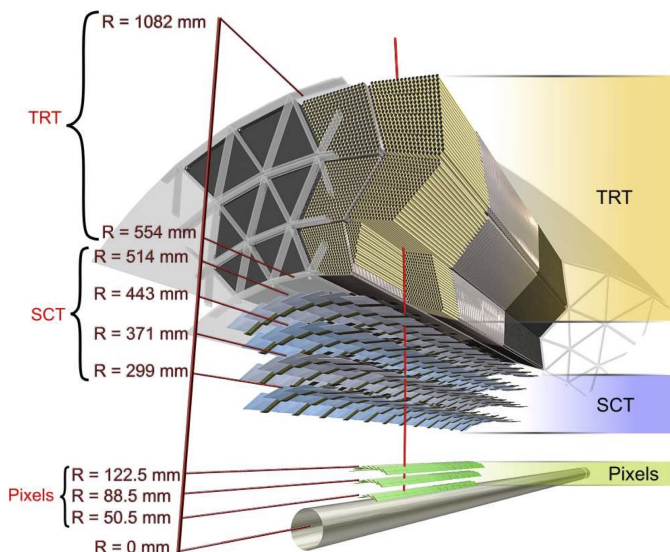


Figure 2.6 – Schematic view of the barrel of the ATLAS inner tracking system [36].

The ID is contained in a cylinder 7 m long and 1.15 m in radius, placed in a 2 T solenoid magnetic field and it is designed to trace charged particles with a minimum moment of 0.1 GeV/c to allow the measurement of the moment through the curvature radius and the reconstruction of the main interaction and decay vertices (both primary and secondary). The innermost part of the ID, which has a radius of about 15 cm, consists of silicon pixels to maximize the precision in the reconstruction of the tracks and the resistance to radiation. The pixel detector records on average three points for each track, which allows a reconstruction of the secondary decay vertices. This detector has a total of approximately 80 million sensitive elements.

The intermediate part, which covers a radius ranging from 30 to 60 cm, uses a microstrip detector (Semi-Conductor Tracker), to provide good spatial resolution. The detection technique of the SCT relies on the same principle as for the pixel detector, however long strips are used compared to the rectangular pixels due to the smaller particle density in the outer layers. It is built around the Pixel detector and is designed to provide eight precision measurements per track, contributing to the measurements of momentum, impact parameter and vertex position. The total number of sensitive items is around 6 million.

The outermost layer ranges from 60 to 95 cm in radius; it is a gas detector (Transition Radiation Tracker) consisting of a set of small diameter tubes, containing Xe (70%), CO₂ (27%), O₂ (3%); it provides a good resolution of the curvature of the track and contributes strongly to its reconstruction.

The tracker contributes to the identification of the electrons, being sensitive to the emission of transition radiation that the particles emit when passing between different materials.

2.2.3 Calorimetric System

Calorimeters must provide good containment for electromagnetic and hadronic showers, they must limit punch-through into the muon system, and finally they must detect the particles that do not lose energy by ionization and are therefore not seen by the internal detector.

It is important that calorimeters cover most possible portion of solid angle; in fact, if a particle pass through a region without instrumentation, it is not detected and its energy contributes to the *Missing Transverse Energy* (MET), the precision of which is essential for identifying and studying weakly interacting particles such as neutrinos and possibly, new BSM particles.

In ATLAS there are two calorimeters: the Electromagnetic Calorimeter (ECAL) and the Hadron Calorimeter (HCAL), as depicted in Figure 2.7 and they cover the range $|\eta| < 4.9$.

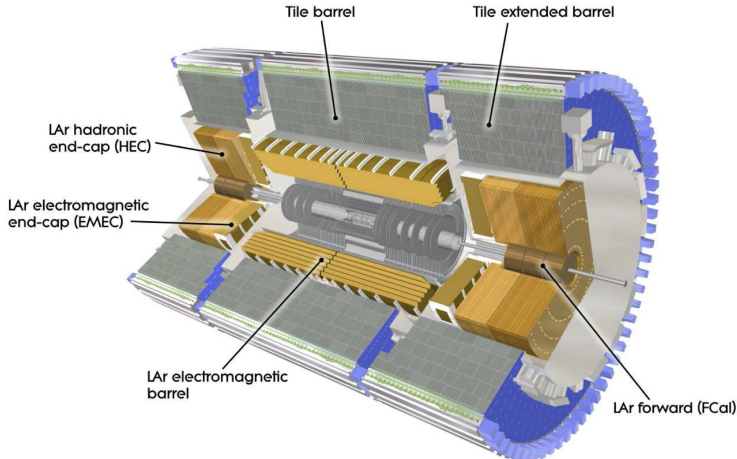


Figure 2.7 – Cut-away view of the ATLAS calorimeter system [36].

The ECAL is divided into a barrel part ($|\eta| < 1.475$) and two end-cap components ($1.375 < |\eta| < 3.2$), each housed in their own cryostat.

It is a lead-LAr detector with accordion-shaped kapton electrodes and lead absorber plates over its full coverage. The accordion geometry provides complete ϕ symmetry without azimuthal cracks. The lead thickness in the absorber plates has been optimized as a function of η in terms of ECAL performance in energy resolution.

A schematic representation of the ECAL in the barrel and its main construction parameters are shown in Figure 2.8.

The outer calorimeter is the HCAL, which is divided in Tile Calorimeter (TileCal), the Hadronic End-cap Calorimeter (HEC) and the Forward Calorimeter (FCal).

LAr technology is also used for the hadronic calorimeters, matching the outer $|\eta|$ limits of end-cap electromagnetic calorimeters. The tile calorimeter barrel covers the region $|\eta| < 1.0$, and its two extended barrels the range $0.8 < |\eta| < 1.7$ and it is a sampling calorimeter using steel as the absorber and scintillating tiles as the active material.

The HEC consists of two independent wheels per end-cap, located directly behind the end-cap electromagnetic calorimeter and the technology is similar to that of the electromagnetic one in the end-cap region, the active medium is LAr, but the absorption medium is made of copper rather than lead. The FCal ($3.1 < |\eta| < 4.9$) is integrated into the end-cap cryostats, as this provides clear benefits in terms of uniformity of the calorimetric coverage as well as reduced radiation background levels in the muon spectrometer. The FCal consists of three modules in each end-cap: the first, made of copper, is optimized for electromagnetic measurements, while the other two, made of tungsten, measure predominantly the energy of hadronic interactions.

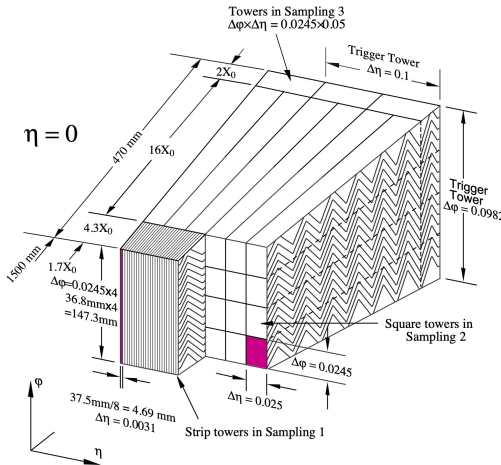


Figure 2.8 – Sketch of the accordion structure of the ECAL [38].

An important quantity to mention is the energy resolution which is parameterized as:

$$\frac{\sigma_E}{E} = \frac{S}{\sqrt{E}} \oplus \frac{N}{E} \oplus C \quad (2.5)$$

The first term represent the stochastic contribution related to the shower evolution, the second term is related to the read-out electronics and the effect of the pile-up. The last term is a constant, due to systematic effects (e.g. mis-calibrations, dead detector material). The dominant source of uncertainty is linked, at low energy, with the high pile-up whereas, at high energy, C becomes the leading uncertainty.

2.2.4 Muon Spectrometer

The calorimeter is surrounded by the Muon Spectrometer (MS) depicted in Figure 2.9, which is placed at the outermost part of the ATLAS detector.

The outer layers are reached by a few types of particles, mainly muons and neutrinos. Those muons ionize with the materials passed through since they are charged particles but the energy, that muons lose by the electromagnetic interaction with other nuclei, is not such as to brake them until absorption. However the MS identify them and measure their momentum.

A series of magnets arranged externally to the calorimeter creates a toroidal-shaped magnetic field that modify the charged particles direction allowing the measurement of the momentum. For muons with $p_T > 30\text{ GeV}$ the measurement is much more precise than the measurement obtained by the internal detector. For lower p_T , on the other hand, the measurement is less accurate, due to the energy loss in the previous layers of

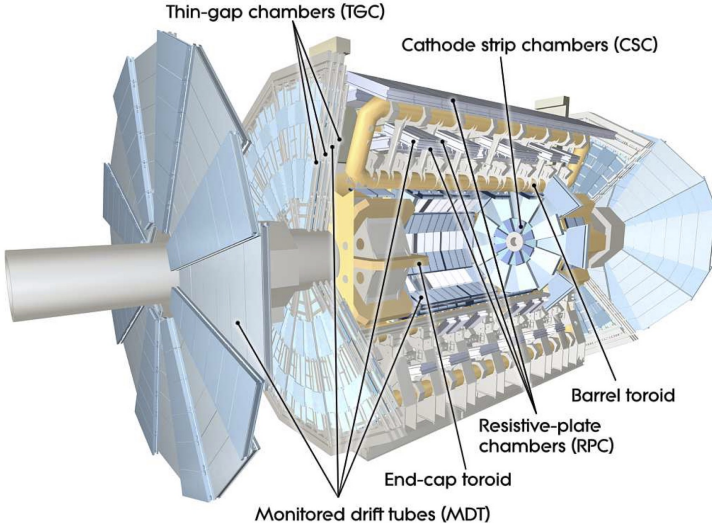


Figure 2.9 – Cut-away view of the ATLAS muon system [36].

the detector and taken in to account to handle *soft muons*, presented in Section 4.2.3. For both the central part and the end-caps, there are two types of detectors:

- a trigger system based on cameras with fast response, such as the *Resistive Plate Chamber* (RPC) and the *Thin Gap Chamber* (TGC),
- precision tracking chambers, such as the *Monitored Drift Tube* (MDT) and the *Cathode Strip Chamber* (CGS).

In the central region ($|\eta| < 1.05$), the RPCs consist of two parallel planes filled with a mixture of gas that ionizes when a muon passes. The HV applied between the plates allows the development of avalanches, along the ionization track towards the anode, which constitutes a signal.

In the end-cap ($1.05 < |\eta| < 2.4$), TGCs are used to complement the RPCs in the triggering system for their good time resolution and rate capability.

The TGC is a multi-wire proportional chamber operated in a highly quenching gas mixture. Both TGCs and RPCs can achieve a read-out time < 25 ns [39].

MDTs are used for muons with $|\eta| < 2$ and they are a series of aluminium tubes, filled with a gas mixture of Argon and CO₂. A central wire serving as anode allows to collect the ions that are formed following the passage of the muon into the gas.

CSCs cover the area where $2 < |\eta| < 2.7$ and are radially oriented proportional multi-wire chambers, i.e. metal chambers containing a system of parallel and perpendicular anodic wires with strips of opposite polarity.

One important point to stress is that this detector measures the characteristics of any charged particle that passes through it and not just muons. For this reason it is possible that other particles that are not muons, such as pions that manage to overcome the calorimeter and detected as muons.

What is presented in this paragraph about the MS is a general overview but much more will be presented in Chapter 3, going deeper on its functioning and its upgrade for HL-LHC.

2.2.5 Trigger and Data Acquisition

Once fully operational, with the high frequency of collisions typical at LHC, an impressive amount of data is produced (40 MHz of p-p bunch collision frequency), which would be impossible to manage without the application of filters. However, the *Trigger and Data Acquisition system* (TDAQ) is able to recognize the interesting events for the study of ATLAS physics.

In Run2 the trigger system consists of two levels of event selection: the *Level-1 trigger* (L1), an hardware trigger that reduces the rate to 100 kHz and a *High-Level Trigger* (HLT), a software trigger, further reducing event rate to 1 kHz.

The Level-1 trigger is composed by three subsystems: the first is the L1 calorimeter trigger (L1Calo), which uses calorimeter information; the second is the L1 muon trigger (L1Muon), which primarily uses TGC and RPC information to make fast decisions on muon items; the third is the L1 topological trigger (L1Topo) that combines information from L1Calo and L1Muon and the Central Trigger Processor (CTP) makes the final decision.

At this point, L1 identifies the *Region of Interest* (RoI) with an event rate reduced below 100 kHz. The RoI are then used by the HLT, which has access to the information of all the sub-detectors, targeting the average rate at 1 kHz.

Finally, the events are assembled into an event record passing to the offline storage facilities for a complete off-line reconstruction [40].

CHAPTER 3

The Trigger system upgrade for High-Luminosity LHC

Since the beginning, the LHC accelerator has faced operating periods and dedicated shut-downs to upgrade the accelerator machine and the detectors. In Figure 3.1 a summary of the LHC timeline for operation and upgrade is shown.

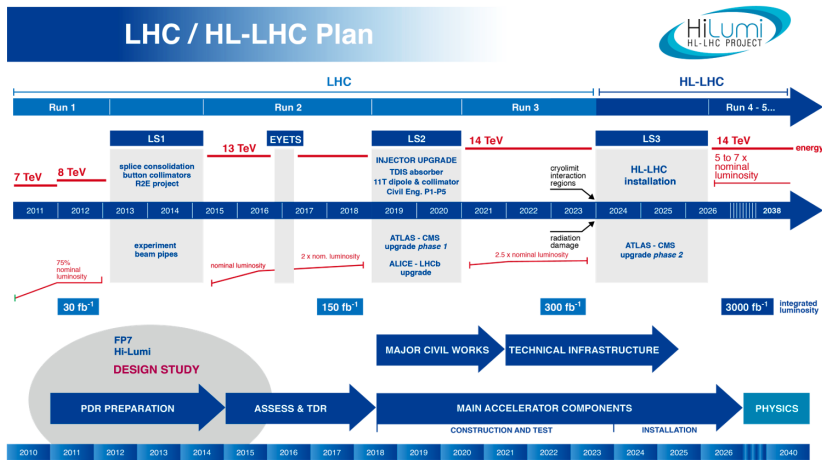


Figure 3.1 – Summary of the LHC timeline for operation and upgrade [41].

At the end of 2018, the LHC was shut-down and for two years it will be upgraded to

reach the center-of-mass energy to its design value of 14 TeV and collect 300 fb^{-1} of data, almost double of the current available statistics of Run2.

After 4 years of duty cycle, the High-Luminosity period of LHC (HL-LHC) will start and aims to bring the integrated luminosity to 3000 fb^{-1} , unlocking several studies, mostly related with rare phenomena, which are impossible to perform with the current statistics.

The main focus of this chapter is the trigger system upgrade for HL-LHC and several studies will be presented.

3.1 ATLAS Barrel Muon Trigger

The muon detector chambers are arranged such that particles from the interaction point traverse three stations of chambers.

The system is subdivided azimuthally into 16 sectors numbered from 1 to 16. The sector number increases in the direction of increasing ϕ with the number 1 corresponding to coordinate $\phi = 0$. The odd sector (called “large sectors”) are located between barrel coils, instead, the even sectors (called “small sectors”) are covered by the coils.

The muon spectrometer consists of three large air-core superconducting toroidal magnets (two end-caps and one barrel) providing a field of approximately 0.5 T.

In the barrel, the chambers are arranged in three concentric cylinders around the beam axis called BI (Barrel Inner), BM (Barrel Middle), and BO (Barrel Outer).

RPC planes are installed in the Middle and Outer stations of the Muon Spectrometer always mechanically associated with MDT precision chambers (except for some “special” chambers).

Two RPC planes are integrated with MDT in the Middle stations and one RPC plane only in the Outer stations.

Schematic drawings of the present ATLAS MS [42], are shown in Figures 3.2 and 3.3. The MS detector and electronics components have been designed for 10 years of operation at a luminosity of $1 \times 10^{34} \text{ cm}^{-2} \text{ s}^{-1}$, corresponding to an integrated luminosity of 1000 fb^{-1} . Conservative safety factors for radiation tolerance and rate capability were taken into account in the original designs, and components have been tested up to and above levels corresponding to the expected doses and rates predicted by simulations multiplied by the safety factors. After the start of LHC operation, detector hit rates and radiation doses could be measured directly, and the previous simulations have been found to agree with the measurements to within a maximum deviation of about 50%.

Based on this observation, the original safety factors were reduced [10], and as a consequence the original irradiation and high-rate tests have qualified the detectors for longer running and higher rates than originally anticipated.

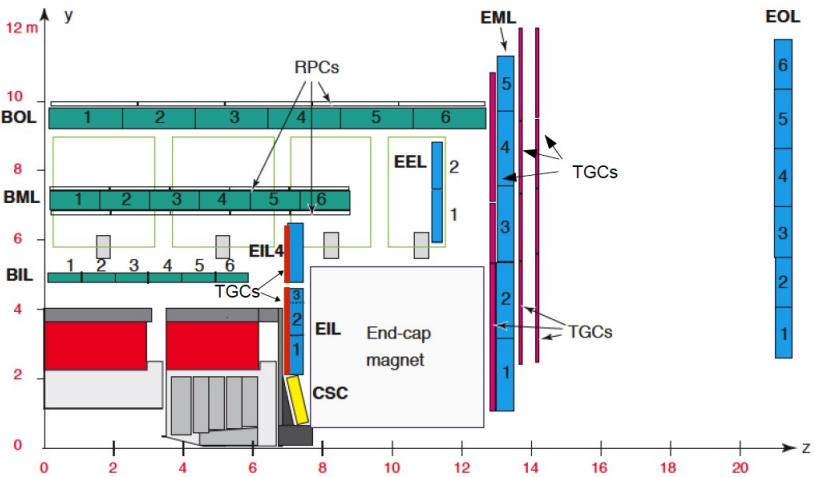
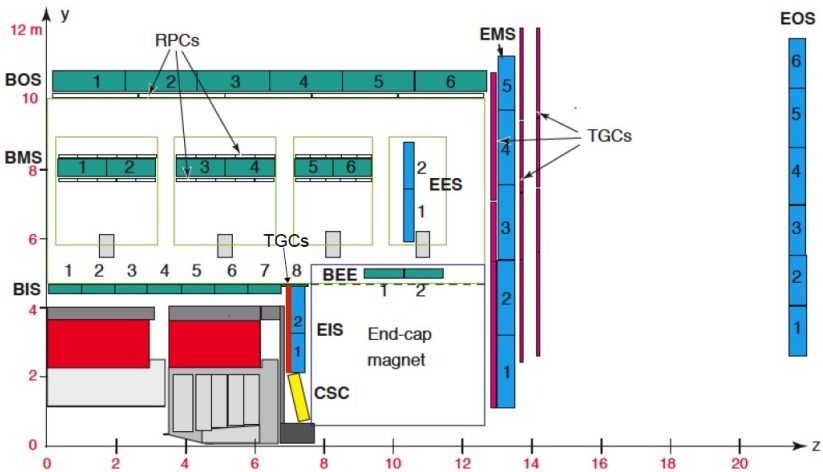


Figure 3.2 – Two R-Z views of the present (Run 1/2) ATLAS muon spectrometer layout. Top: One of the azimuthal sectors that contain the barrel toroid coils (small sector). Bottom: One of the sectors in-between the barrel toroid coils (large sector) [42].

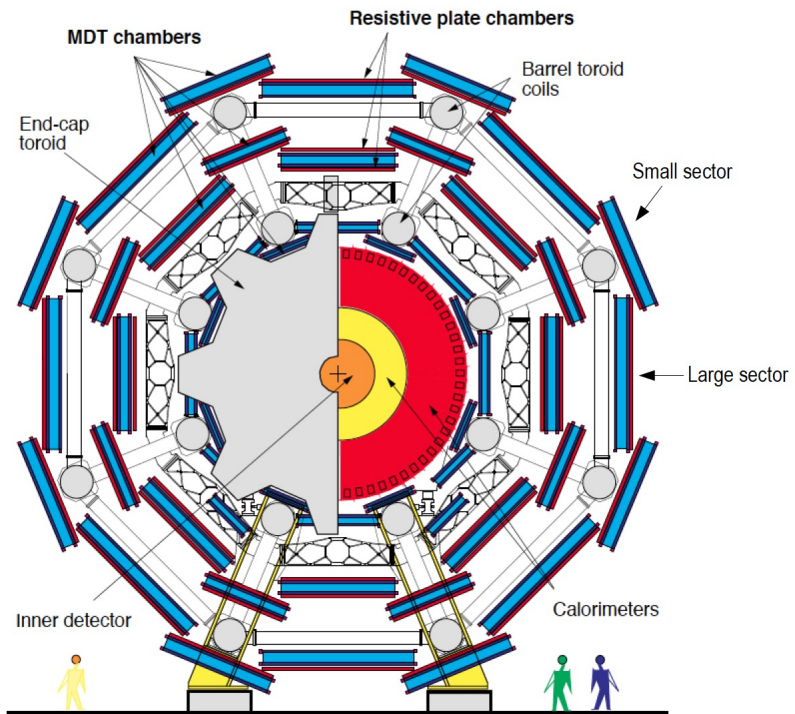


Figure 3.3 – View of the present (Run 1/2) ATLAS muon spectrometer barrel layout in the plane transverse to the beam axis (X-Y plane) [42].

3.2 BI upgrade for Phase II

In the Phase-I upgrade, foreseen for LS2, the Small Wheels will be replaced by the New Small Wheels (NSW) [43] using small-strip TGC (sTGC) and Micro-Mesh Gaseous Structure (MicroMeGaS or Micromegas, MM for short) chambers used for both triggering and precision tracking.

At the time of the Phase-II upgrade, there will thus be no CSC chambers any more in the detector, nor will there be the Small Wheel MDT chambers, which are the ones closest to the beam line and exposed to the highest rates. Also in LS2, the BIS7 and BIS8 MDT chambers will be replaced by integrated BIS78 stations of new RPC and small diameter MDT (sMDT) chambers to enhance the trigger coverage in this region [44].

Schematic drawings of the ATLAS MS with the new detectors that will be installed in the Phase-I and Phase-II upgrades are shown in Figure 3.4.

To maintain a high trigger efficiency, new RPC chambers with increased rate capability will be installed on the inner (BI) MDT chambers of the barrel. This addresses a fundamental issue of the present (old) RPC chambers: to ensure their continued operation at the HL-LHC, these chambers will have to be operated at reduced performance (i.e. efficiency), in order to respect the original design limits on currents and integrated charge. This can be achieved by reducing the gas gain through lowering the operating voltages. In the areas of high backgrounds, the gas gain will have to be reduced to such low levels that hit inefficiencies up to 35% will be encountered. This would reduce the trigger efficiency in the barrel region to an unacceptable level if no compensating measures were taken. In addition, due to changes in regulations, the present gas mixture used in ATLAS RPCs may need to be replaced by one with lower global-warming potential (GWP). Unless new gas mixtures are found in time, this too will imply operation of old RPCs at a reduced efficiency. Despite the lower single-hit efficiencies, a high trigger efficiency and purity can be maintained by loosening the requirements on hit coincidences in the old chambers, if at the same time a coincidence with the new BI RPC chambers is introduced. The installation of these chambers will also close most of the acceptance holes of the present barrel muon trigger, which amount to more than 20% of the $\eta - \phi$ coverage for $\eta < 1.05$ (see Section 3.4).

Adding new RPC chambers in the barrel is challenging in terms of available space and installation. In the small sectors, the BI RPC chambers can only be installed if the present MDT chambers are replaced by new sMDT chambers with reduced overall thickness so that the sMDT chambers and the new RPCs fit in the same envelope as the original MDT chambers. In the large sectors there is sufficient space available to add the new RPC chambers without replacing the MDTs, if on-detector services are re-arranged. The retrofitting of selected RPC chambers in the BM and BO layer in the areas of high rate at $\eta > 0.8$, namely the BML7 and BOL6 chambers, is a small additional upgrade. The MDT+RPC stations will be temporarily removed from the detector to replace the

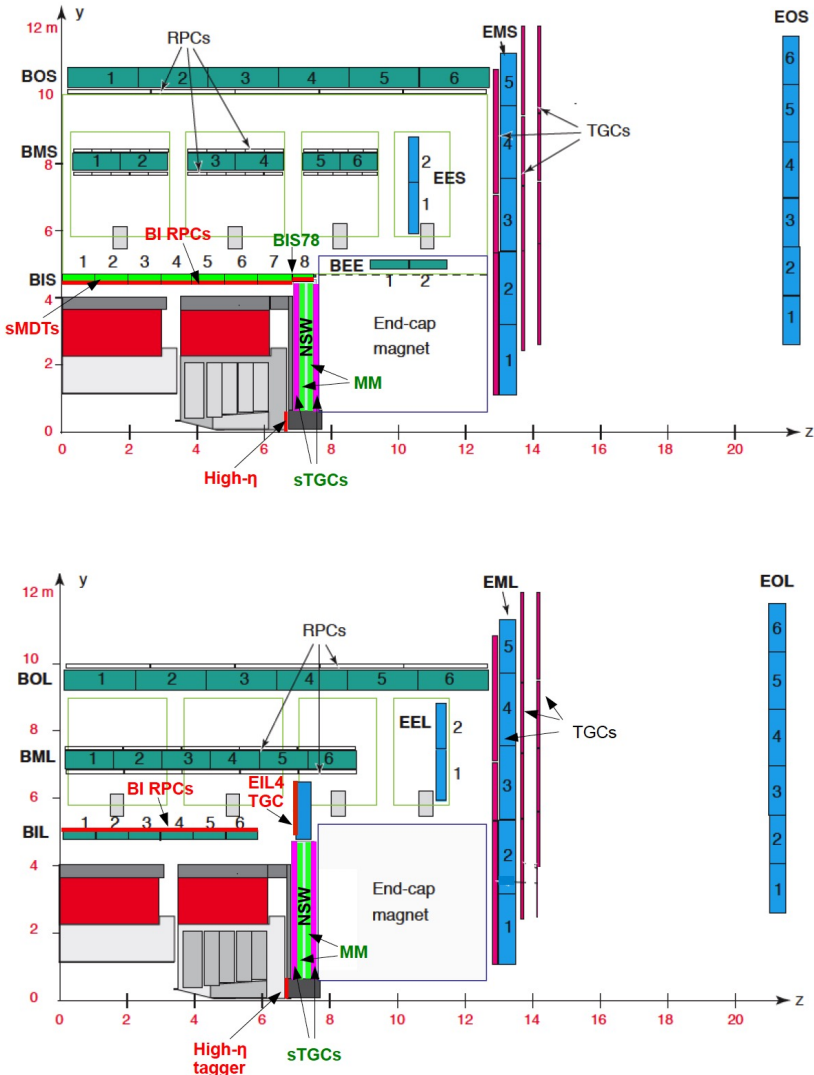


Figure 3.4 – Two R-Z views of the Phase-II ATLAS muon spectrometer layout showing a small sector (top) and a large sector (bottom). The drawings show the new detectors to be added in the Phase-II upgrade, including the addition of the high- η tagger (red text: BI RPC, sMDT, EIL4 TGC, high- η tagger), those to be installed during LS2 (green text: Micromegas and sTGC in the New Small Wheel and BIS78 RPC and sMDT), and those that will remain unchanged from the Run 1 layout (black text) [42].

front-end electronics and the readout panels, so that the chambers can be run at reduced HV without efficiency loss.

In the Section 3.4.1 it will be presented a study performed on the refurbish of BM and BO chambers and the installation of BI chambers in the rail sectors 11 and 15.

The retrofitting can only be done outside the experimental cavern, on the surface, since it requires the disassembly of the RPC chambers. The retrofitting of the BO chambers does not fit into the LS3 schedule because it would interfere with the BI chamber upgrade, and will likely be performed, at least partly, in winter shutdowns after LS3.

The main limitations of the RPC system for operation at the HL-LHC are related to the chambers, owing to the more than a factor of seven higher luminosity than the chambers were designed for. The RPC rate capability depends on the total charge delivered per count, which, for the present RPCs, is 30 pC.

As a consequence, the single-gap efficiency will have to be reduced on average by 15%, and by 35% at large η . This efficiency loss will be compensated by installing a new layer of trigger chambers in the BI layer, increasing the overall barrel trigger redundancy.

To operate reliably at the HL-LHC, with high acceptance and efficiency and maintaining, the high trigger selectivity of the present system, several upgrades are required for the RPC system:

- A new inner layer of BI RPC chambers will be added to the spectrometer. This will recover most of the current geometrical acceptance holes. The redundancy of the system will be greatly enhanced, so that full trigger efficiency can be maintained even if the old RPCs have to be operated at reduced efficiency, either to limit the effects of ageing or because the use of a different gas mixture is enforced. The BI RPCs will be new-generation RPCs with 1 mm gas gaps and high-sensitivity front-end electronics.
- The trigger and readout electronics (Pad and splitter boxes) have to be replaced in order to make the RPC system compliant with the Phase-II ATLAS trigger and readout scheme. The entire electronics chain, except for the front-end boards, will be replaced. The Pads will be replaced by the new data collector and transmitter (DCT) boards that will send all data off the detector to the counting room USA15 where the trigger and readout logic will be performed.
- In a worst-case scenario for the required reduction of efficiency of the old RPCs, a reduction of the trigger efficiency may still occur even after the BI RPC installation, in the region of $|\eta| > 0.8$. This efficiency loss can be recovered by retrofitting a limited number of BO chambers in that region. The retrofitting comprises replacing the original front-end electronics by the new BI version, and replacing the readout strip panels.

3.2.1 RPC upgrade

The BI system is designed to increase the trigger acceptance and the trigger efficiency, by loosening the requirements on the number of hits in the BM and BO chambers and, at the same time, adding the requirement of a coincidence with the BI layer. Any coincidences of hits in at least three chambers out of four (counting one BI, two BM, and one BO) will be accepted. Two-chamber BI-BO coincidences will be used to cover the remaining acceptance holes. Details of the Phase-II trigger algorithms and their performance are discussed in Section 3.3. Figure 3.5 illustrates the recovery of acceptance and efficiency obtained with the Phase-II trigger including the BI RPCs in a worst-case scenario in which the single-hit efficiency of the old RPC is reduced by 15–35% as a function of $|\eta|$, depending on the rate to which each chamber is exposed.

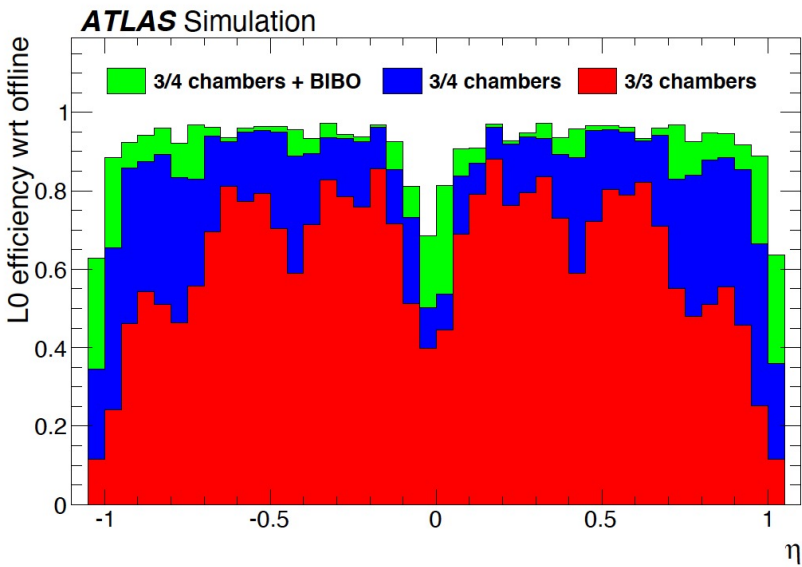


Figure 3.5 – Efficiency times acceptance of the L0 barrel trigger for reconstructed muons with $p_T = 25$ GeV as a function of η , assuming the worst-case scenario [42].

The new BI RPC chambers will have three sensitive gas gaps that are read out independently. A majority logic requiring hits in at least two out of three planes provides high efficiency while suppressing the rate of random coincidences due to uncorrelated hits from photons and neutrons. This is necessary, for instance, to keep the rate of BI-BO coincidences at an acceptable level.

A major re-design of the RPC technology started around the year 2010, mainly aiming at a better rate capability and ageing behaviour. The new design is based on a reduced thickness of the gas gaps (from 2 mm to 1 mm) and of the resistive electrodes (from 1.8

mm to 1 mm), and on the use of a new generation of low-noise high-sensitivity amplifiers. Using these amplifiers, full efficiency can be achieved for a lower voltage across the gas gap, thus transferring part of the amplification from the gas avalanche to the electronics. In this way, the RPCs can be operated at a reduced charge per avalanche, reducing the detector current and thus improving rate capability and ageing.

A detail view of the positions of the BI RPCs in ATLAS is shown in Figure 3.6.

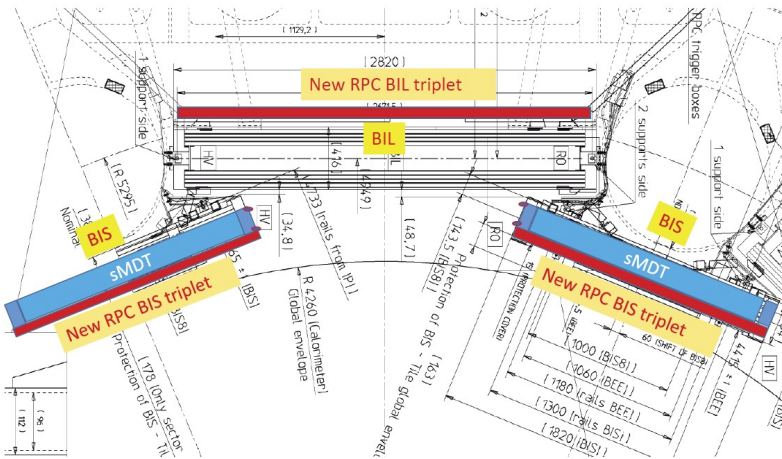


Figure 3.6 – X-Y view of the inner barrel layer, indicating the positions of the BI RPCs (red) and BIS sMDTs (blue) in the small and large sectors [42].

In the small sectors (BIS), due to the tight space limitations, the MDT chambers need to be replaced by new small-diameter MDT (sMDT) chambers with half the tube diameter (15 mm instead of 30 mm) in order to create space for the RPCs on the inside of the sMDT chambers. In the large sectors (BIL), the new RPCs will be installed on the outside of the existing MDTs. The layout of the new BI RPCs leaves the necessary holes and cut-outs for the existing MDT alignment lines and for detector services. It comprises 272 triplet RPC chambers, for a total area of about 470 m². Acceptance studies based on a realistic description of the BI RPC geometry show a geometrical acceptance of the BI RPC chambers of 91% for reconstructed muons with $|\eta| < 1.05$, compared to 95% for the MDT chambers. This results in a barrel trigger acceptance of 96%.

Each detector layer of the triplets is read out on both surfaces by orthogonal strip panels, providing η and ϕ measurements. The compact triplet structure and the use of highly sensitive amplifiers require a complete isolation of individual layers from each other. The choice of strip pitches, 24–26 mm depending on the chamber type, has been constrained by the performance requirements, the strip impedance, and cost considerations. The total number of readout channels is about 8700.

3.2.2 Trigger scheme

All the hits from RPC detectors will be available to the barrel Sector Logic board that uses them to generate barrel trigger candidates. The new BI RPCs increase the geometrical acceptance of the present barrel muon trigger and its robustness against inefficiencies of the old BM and BO RPCs caused by the reduced operating voltages necessary to ensure their longevity.

The RPC trigger will use nine measurement planes, provided by four layers of RPC chambers: one BI triplet (RPC0), two BM doublets (RPC1 and RPC2), and one BO doublet (RPC3). Figure 3.7 shows the positions of the BI, BM, and BO RPC chambers in a small barrel sector together with the MDT chambers. The acceptance holes in the BM layer, caused by the magnet coils and their supports, are also visible.

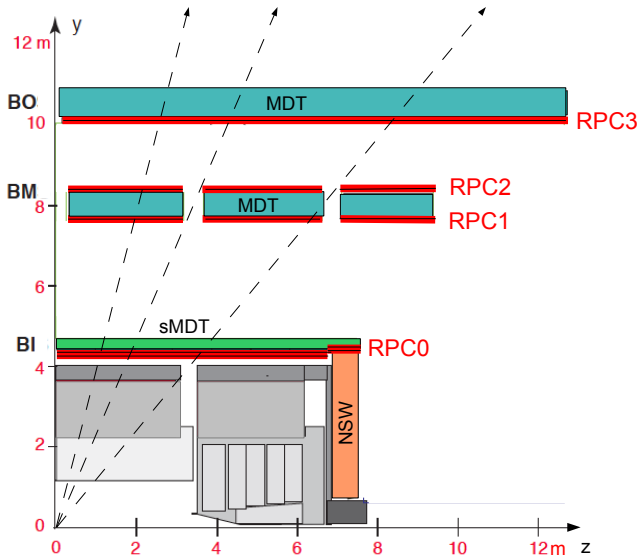


Figure 3.7 – Transverse section of a small sector in the barrel region, showing the four layers of RPC chambers (RPC0,1,2,3), as well as the MDT chambers in the barrel-inner (BI), barrel-middle (BM), and barrel-outer (BO) layers. The three dashed lines represent muon trajectories traversing four, two, and three RPC chambers [42].

To take advantage of the redundancy of detector planes, a trigger algorithm that does not make use of a fixed pivot plane (as in present ATLAS muon trigger) has been developed. This makes it possible to define different trigger coincidence logic schemes.

These schemes (summarised in Table 3.1 and illustrated in Figure 3.8) are based on different requirements on the four layers of RPC chambers:

- 3/3 chambers. Hits in at least three out of four planes of the RPC1+RPC2 chambers and in at least one out of two planes of RPC3. This is equivalent to the present high-pT trigger.
- 3/4 chambers. The previous requirement in a logical OR with the requirement of hits in at least two planes out of three in RPC0 and in at least three planes out of six in RPC1+RPC2+RPC3. In this way, all combinations of three-chamber coincidences (satisfying the above hit requirements) are accepted.
- 3/4 chambers + BI-BO. The previous requirement in a logical OR with the requirement of at least two hits in RPC0 and at least one hit in RPC3. This enhances the trigger coverage in the regions where no BM RPCs are installed due to the mechanical support structure of the toroid coils. The BI-BO coincidence is expected to be prone to accidental coincidences of uncorrelated background hits that are negligible in three-chamber coincidences. In the baseline version of this trigger, BI-BO coincidences are used in the whole barrel region, but can be limited to the BM acceptance gaps, if the muon trigger rate in the barrel gets too high.

Trigger	Requirement
3/3 chambers	$3[\text{RPC1+RPC2}] \text{ AND } 1[\text{RPC3}]$
3/4 chambers	$(3[\text{RPC1+RPC2}] \text{ AND } 1[\text{RPC3}]) \text{ OR } (2[\text{RPC0}] \text{ AND } 3[\text{RPC1+RPC2+RPC3}])$
3/4 ch.+BI&BO	$(3[\text{RPC1+RPC2}] \text{ AND } 1[\text{RPC3}]) \text{ OR } (2[\text{RPC0}] \text{ AND } 3[\text{RPC1+RPC2+RPC3}]) \text{ OR } (2[\text{RPC0}] \text{ AND } 1[\text{RPC3}])$

Table 3.1 – The hit requirements used in different RPC triggers. The left column shows the short name used in the text. The right column gives the coincidence scheme used for the selection logic. The notation $N[\text{RPC}_i+\text{RPC}_j+\dots]$ indicates a majority requirement of hits in at least N planes out of all the possible planes available in RPC chambers RPC_i , RPC_j, \dots with $i, j, \dots \in \{0, 1, 2, 3\}$.

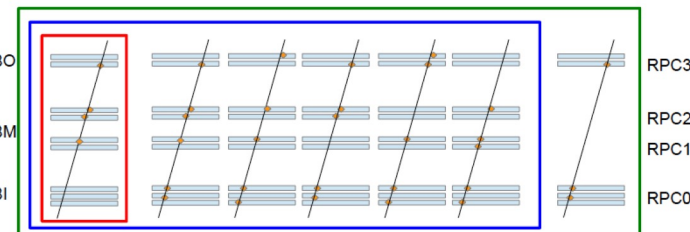


Figure 3.8 – Graphic view of the coincidence scheme used for the selection logic. High-Pt (3/3 chambers) in red, 3/4 chambers in blue, 3/4 ch.+BI&BO in green.

3.3 Hit digitization in the BI region

Since at the present time the new chambers in the BI region are not yet installed, the simulation performed for this work takes into account the presence of hits in the BI RPC chambers exploiting the true hits, recorded by the MDT chambers in the BI region, and treating them as hits of the future RPC chambers.

In this work, it has been used the the common framework `muTrigNt_write` [45] that includes a realistic digitization. This code reproduces the dimensions of the new BI RPC chambers and, given as input the true MDT hits, it checks if the hits are in the geometric acceptance.

The code allows generating strips (both in η and ϕ coordinates) as well and thus to digitize the true MDT hit recording its as a hit in the middle of the strip. This `muTrigNt_write` is also able to simulate the trigger efficiencies as described in Sec 3.4. They have been calculated considering muons reconstructed in $\eta < 1.05$ by the offline reconstruction, using a single-muon Monte Carlo sample with fixed $p_T = 50$ GeV and uniform distributions in η and ϕ . It is the official Muon-phase2 sample `mc15_14TeV.422063.ParticleGun_single_mu` containing 50K events, produced with the ITk (Inner Traker) simulation and with the layout of Run-I muons, that differs compared to the layout of Run-II muons because the feet and the elevator chambers are missing. The simulation implements a more realistic digitization that produces:

- cluster size, strip number and the associated coordinates of the strips (Section 3.3.1);
- timing (Section 3.3.2);
- BI and BMBO Efficiencies (Section 3.4);

3.3.1 The cluster size model

A single discharge in the gas volume can induce a signal in more than one RPC strip (i.e. occurs a so-called *cluster*), this is due to the charge sharing. The number of RPC strips fired in temporal coincidence is called *cluster size*. The cluster size is a relevant parameter for RPC detector and it must be strictly monitored to ensure a full trigger efficiency. The cluster size is simulated using a Gaussian charge distribution, with fixed width and centered on the true MDT hit that is induced on the strips [47]. This function is defined as:

$$G(z) = f(A) \cdot \text{erf} \left(\frac{\mu - z}{\sigma \sqrt{2}} \right) \quad (3.1)$$

where the amplitude distribution $f(A)$ is variable with an exponential decreasing tail $f(A) = e^{-\frac{A}{\tau}}$, with the parameters $\tau = 0.8$ and random A , fixed width $\sigma = 16$ mm and μ is the z - coordinate of the hit.

When the charge integrated over a strip exceeds a certain threshold (0.2 in this simulation), then the strip is switched on.

This is not a strictly physical model but a decreasing exponential is useful to produce the expected tail, unless to use a more realistic model for amplitudes based on experimental studies. A picture of the model used in this simulation is illustrated in Figure 3.9. Clus-

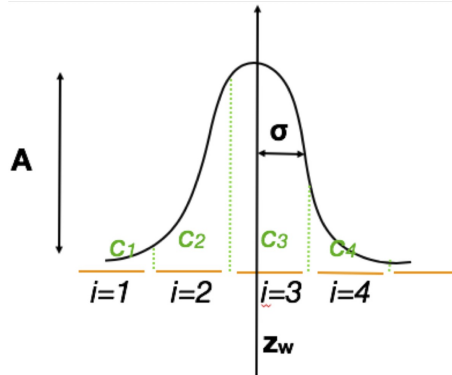


Figure 3.9 – Cluster size model used in the simulation. C_i is the charge integrated over a strip i . Some other parameters are the strip pitch z_w (22 mm), random amplitude A and width σ . When the charge integrated over a strip exceeds a certain threshold, the strip is switched on [47].

ter size is given by the number of strips fired at the same time. It depends on the absolute value of charge integrated over a strip but it also depends on the position of the true hit. Originally, the RPC hit is fixed to be at the center of the strip and the true MDT hit belongs to one strip only but in this simulation, it would be possible to have many strips fired at the same time using the relation: $\text{GlobPos}_i = \text{GlobPos}_{i,\text{true}} \pm \text{strip_center}_i$. The resulting cluster size distribution is shown in Figure 3.10.

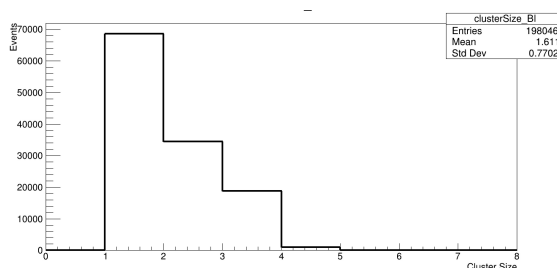


Figure 3.10 – Cluster size distribution obtained with the model and parameters illustrated in this section. The average value is 1.6.

Looking at the hit distribution in Figure 3.11(a) for the η layer and Figure 3.11(b) for the ϕ layer, it is possible to see that:

- CS=0 never possible by definition, one hit corresponds at least at one fired strip;
- CS=1 the hit distribution is uniform, because the integrated charge is less than the fixed threshold;
- CS=2 mostly when the truth hit is far from the strip center and at the strip edge;
- CS=3 mostly when the truth hit is far from the strip edge and at the strip center;
- CS>3 are rare events, but they follow the same pattern.

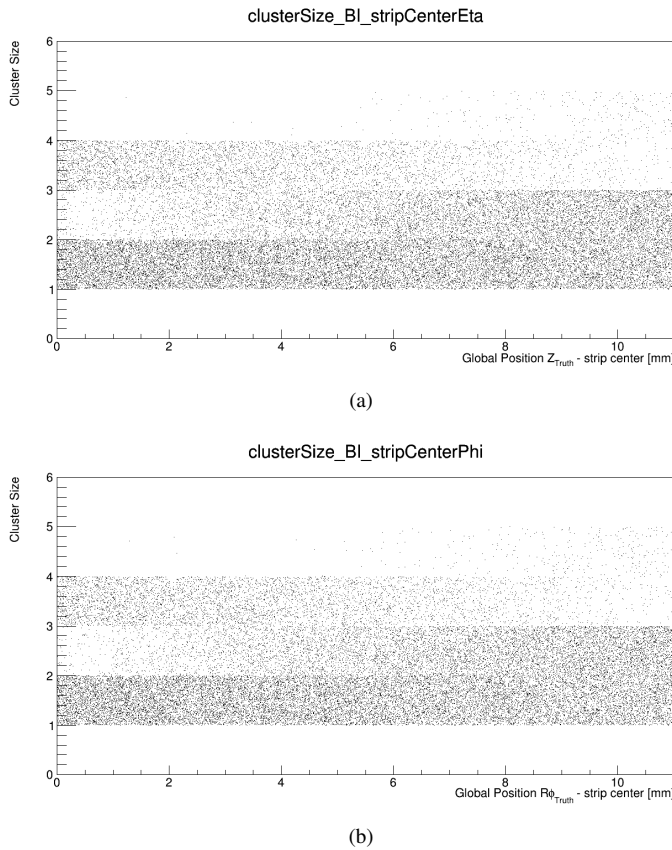


Figure 3.11 – RPC hit distribution GlobPos_i for a) strips along η and b) strips along $R\phi$.

Strips in η and ϕ layers are orthogonal to each other and it is possible to see how they are arranged as a function of the Global Position in the BI region of the ATLAS detector. In particular, in Figure 3.12(a) strips oriented along η are ordered in such a way that the strip number one is the inner strip, while Figure 3.12(b) shows that strips oriented along ϕ are always oriented with increasing ϕ .

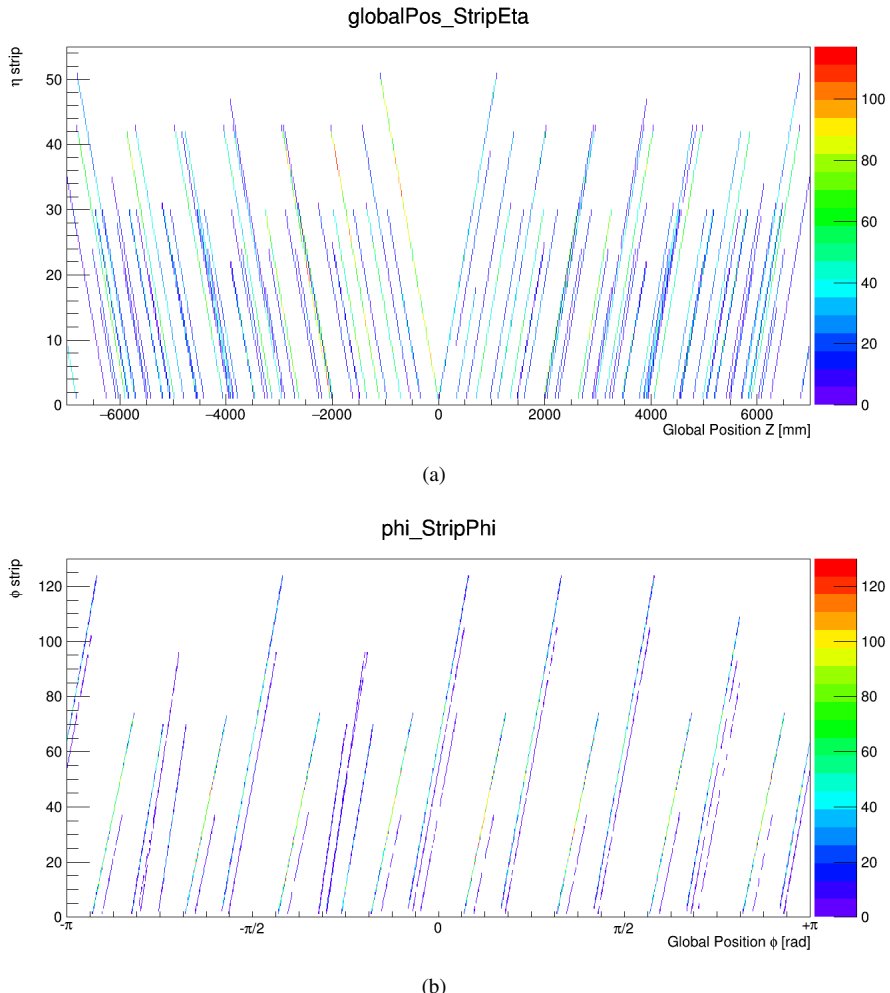


Figure 3.12 – Arrangement of strips in the a) η layer and b) ϕ layer as a function of the Global Position in the BI region of the ATLAS detector.

Tables 3.1(a) and 3.1(b) summarise the main chamber parameters of the expected layout for the Phase II upgrade. Strip and front-end board entries are based on the assumptions of a 20 mm pitch and eight channels per board.

Figure 3.13 shows the number of η and ϕ strips switched on in the simulation. It is possible to verify that the simulation developed for this work follows the requirements of the Phase II upgrade for BI RPCs to be realistic and reliable as much as possible.

RPC type	BIL-A	BIL-B	BIL-C	BIL-D	BIL-K	BIL-E	BIL-F	BIL-G	BIL-H	BIL-I	BIL-J
# of units	72	2	4	2	2	14	2	8	6	2	2
# of layers	3	3	3	3	3	3	3	3	3	3	3
length in Z (mm)	640	510	365	600	220	640	540	450	310	370	370
width in ϕ (mm)	2750	2750	2750	2750	2750	2380	2380	2300	2100	1850	1700
η strip pitch (mm)	18.4	19.2	19.7	17.2	21.3	18.4	20.4	16.7	16.3	20.0	20.0
ϕ strip pitch (mm)	21.1	21.1	21.1	21.1	21.1	20.8	20.8	21.6	21.4	20.5	20.6
# η strips/layer	32	32	16	32	8	32	24	24	16	16	16
# η strips/unit	96	96	48	96	24	96	72	72	48	48	48
# ϕ strips/layer	128	128	128	128	128	112	112	104	96	88	80
# ϕ strips/unit	408	408	408	408	408	360	360	336	312	288	264
area/layer (m^2)	1.76	1.40	1.00	1.65	0.61	1.52	1.29	1.04	0.65	0.68	0.63
gap area (m^2)	1.61	1.25	0.86	1.50	0.47	1.39	1.15	0.91	0.54	0.58	0.54
Gas volume/layer (l)	4.82	3.76	2.59	4.49	1.41	4.16	3.46	2.73	1.63	1.75	1.61
# FE cards/layer η	4	4	2	4	1	4	3	3	2	2	2
# FE cards/layer ϕ	16	16	16	16	16	14	14	13	12	11	10

RPC type	BIR-A	BIR-B	BIR-C	BIR-D	BIM-A	BIM-B	BIS-A	BIS-B
# of units	4	8	8	4	12	24	16	80
# of layers	3	3	3	3	3	3	3	3
length in Z (mm)	780	916	1104	735	437	495	1096	916
width in ϕ (mm)	2099	1251	819	1260	1536	1536	1820	1820
η strip pitch (mm)	18.3/22.8	21.7	22.0	21.4	16.1/24.2	18.5/27.8	21.8	21.7
ϕ strip pitch (mm)	21.3	21.4	19.2/24.0	21.6	20.6	20.6	20.1	20.1
# η strips/layer	40/32	40	48	32	24/16	24/16	48	40
# η strips/unit	120/96	144	168	96	72	72	168	120
# ϕ strips/layer	96	56	40/32	56	72	72	88	88
# ϕ strips/unit	288	168	120/96	168	216	216	264	264
area/layer (m^2)	1.64	1.15	0.90	0.93	0.67	0.76	2.00	1.67
gap area (m^2)	1.51	1.05	0.82	0.84	0.58	0.67	1.86	1.54
Gas volume/layer (l)	4.52	3.15	2.45	2.51	1.75	2.01	5.59	4.63
# FE cards/layer η	5/4	5	6	4	3/2	3/2	6	5
# FE cards/layer ϕ	12	8	5/4	7	9	9	11	11

Table 3.2 – Main parameters of a) the BIL RPC chambers and b) the BIR/BIM/BIS RPC chambers [42].

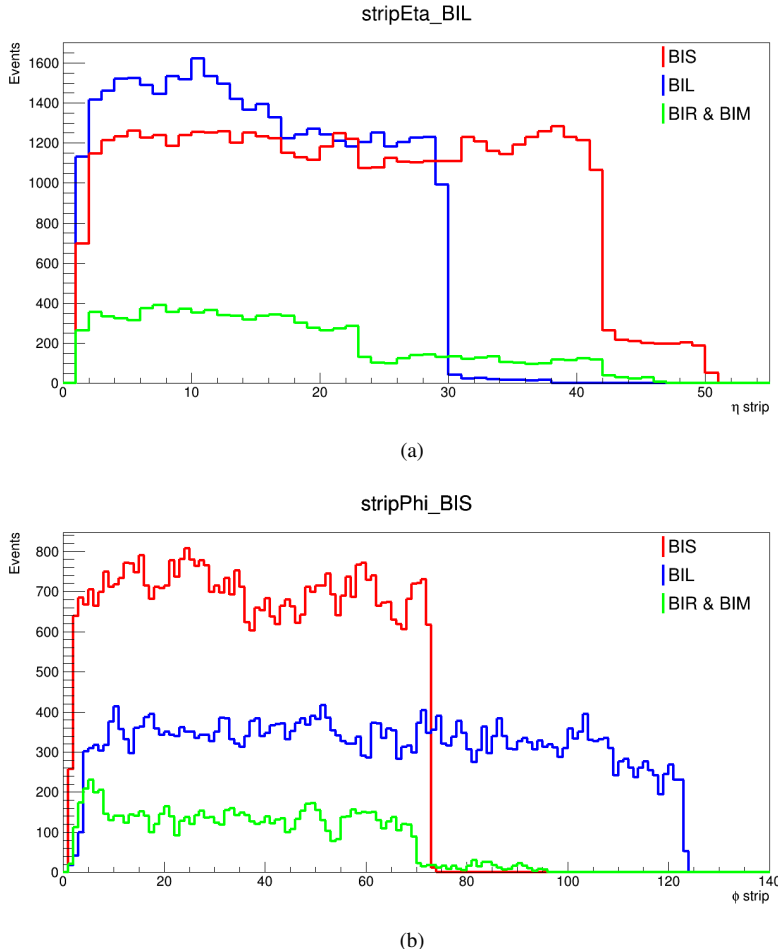


Figure 3.13 – Number of η and ϕ strips switched on for different chambers: BIS in red, BIL in blue, BIR & BIM in green.

3.3.2 Timing

Another important variable is the time taken for the particle to pass through the detector. It is important because it is one of the discriminating variables in the algorithm's selection of hits. Hits recorded in the bunch crossing event are considered and not all the hits previously recorded. Therefore, all hits outside 25 ns coincidence window around the bunch crossing of interest are excluded.

In order to simulate the new RPCs one has to take into account several effects and apply

an appropriate correction and extract a digital readout.

The final formula used to extract digitized time in which the hit is recorded by the detector is:

$$t_{hit} = \text{int}^{\text{1}}\left(\frac{t_{true} + t_{Gauss} + t_{FE} - t_{cal}}{\Delta t}\right)\Delta t \quad (3.2)$$

- t_{true} is the true hit recorded by the MDT;
- Δt is the sampling rate (0.3 ns). The final t_{hit} must be a multiple of the sampling rate to have a digitization;
- t_{Gauss} is a Gaussian term that reproduces the fluctuations in the RPC signal (smearing 0.4 ns);
- t_{FE} is the propagation of the signal along the strip to the FE electronics assuming that the signal speed on the layer is 200 mm/ns;
- t_{cal} is the calibration offset. The true hit timing is recorded referring to the time of the collision on the MDT tubes. To report the timing centered around 0, it was necessary to subtract the time of flight of the particle assuming time to be calibrated with prompt muons crossing the center of the strip at $t = 0$.

Figure 3.14 shows the digitized time associated to the RPC hit calculated using the Equation 3.2. The tail of the distribution is given by low p_T muons that produce secondary hits.

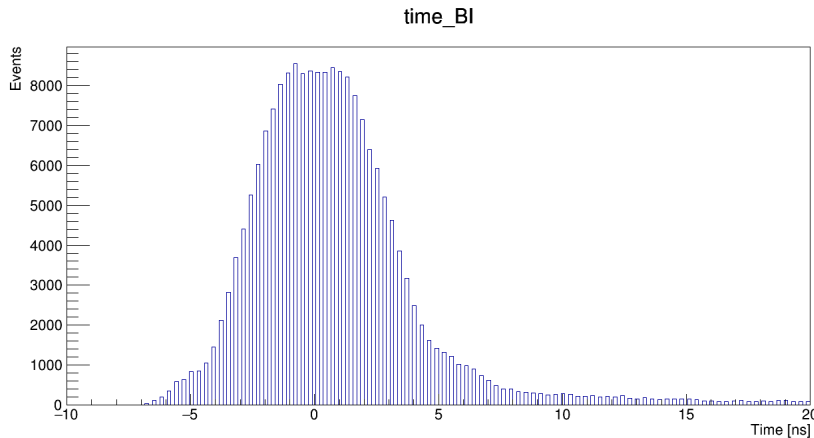


Figure 3.14 – Digitized time associated to the RPC hit. The tail of the distribution is given by low p_T muons that produce secondary hits

3.4 L0 barrel trigger efficiency

The performance of the barrel muon trigger was studied for a fixed transverse momentum threshold: $p_T > 10 \text{ GeV}$ [48] and with the hit digitization described in the previous sections.

To study the robustness of the trigger against possible efficiency reductions of the old RPCs in the BM and BO layers, the simulation was performed in the so-called "worst-case scenario" that introduces inefficiencies depending on the station type and sector and summarised in Table 3.3. It includes inefficiencies due to a reduction of the high voltage of the BM and BO RPCs such that the expected RPC current is always below the safe operation limit. The trigger efficiency times acceptance for each trigger logic

Station Name	StationEta							
	1	2	3	4	5	6	7	8
BOL	0.90	0.90	0.82	0.82	0.76	0.74	-	-
BOS/BOG/BOF	0.89	0.90	0.90	0.90	0.89	0.66	0.60	0.60
BML	0.88	0.88	0.88	0.83	0.56	0.56	0.60	-
BMS	0.90	0.90	0.90	0.87	0.81	0.81	-	-

Table 3.3 – Efficiency for each station and sector of the barrel muon trigger in the "worst-case scenario". This scenario includes inefficiencies due to a reduction of the HV of the BM and BO RPC [48].

scheme is listed in Table 3.4 and it is defined as the fraction of reconstructed muons that are accepted by the trigger, using the simulation that includes the RPC detector efficiency. The trigger efficiency times acceptance is also presented in Figure 3.15. Adding the new BI RPC layer greatly reduces the dependence of the trigger efficiency on the hit efficiency of the old RPCs.

BM and BO efficiency (%)	Trigger efficiency x acceptance (%)		
	3/3 chambers	3/4 chambers	3/4 chambers + BIBO
WCS	58.78	83.27	91.89

Table 3.4 – Efficiency times acceptance for the L0 barrel trigger for each trigger logic scheme, assuming the worst-case scenario with the hit digitization .

Starting from the WCS scenario, other studies have been performed on the L0 barrel trigger efficiency using simulations with RPC stations in various operational conditions, in particular the refurbish of BM and BO chambers (Section 3.4.1) and about the installation of BI chambers in the rail sectors 11 and 15 (Section 3.4.2).

¹The *int* function takes the integer part of a natural number.

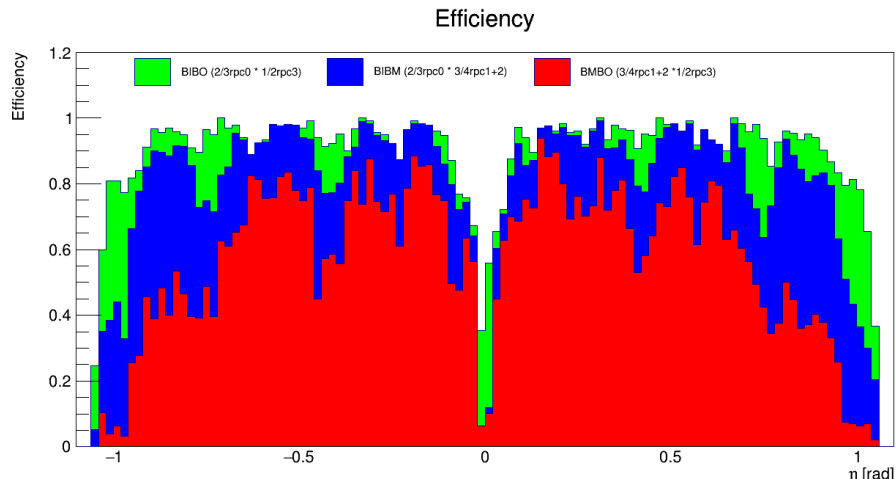


Figure 3.15 – Efficiency times acceptance of the L0 barrel trigger for each trigger logic scheme, assuming the worst-case scenario with the hit digitization.

3.4.1 BM and BO retrofitting

In the first case presented, efficiencies of the "worst-case scenario" summarised in Table 3.3, are used, except for the following stations, setted to 100% efficiency:

1. BML 7,
2. BOL 6,
3. BOS 6,
4. BOL 5.

At this stage, an essential step is to understand what would be the impact of the legacy BM/BO chambers with the new electronics.

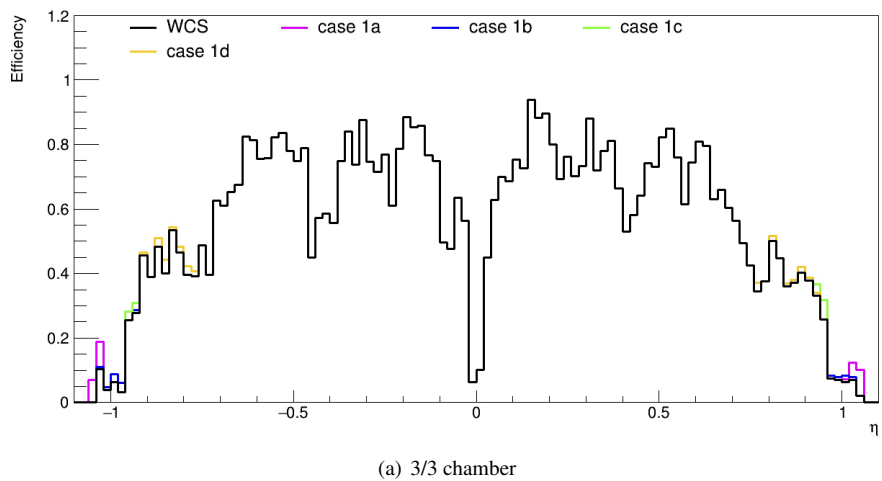
The products of muon trigger efficiency and acceptance for the BM and BO retrofitting are listed in Table 3.5.

The trigger efficiency times acceptance is also presented in Figure 3.16 that compare the "worst-case scenario" with all the variants of the WCS, in which some stations are fixed to 100% efficiency.

In the first analysed case, the most relevant effect on the trigger efficiency times acceptance is on the 3/4 chambers logic scheme, in particular for the Case 1b (BOL 6 100%) the variation is +1.08% compared to the "worst-case scenario".

BM and BO efficiency (%)	Trigger efficiency x acceptance (%)		
	3/3 chambers	3/4 chambers	3/4 chambers + BIBO
WCS	58.78	83.27	91.89
Case 1a (BML 7 100%)	+0.22	+0.26	+0.14
Case 1b (BOL 6 100%)	+0.13	+1.08	+0.53
Case 1c (BOS 6 100%)	+0.16	+0.51	+0.63
Case 1d (BOL 5 100%)	+0.23	+0.82	+0.41

Table 3.5 – Efficiency times acceptance for the L0 barrel trigger for different assumptions on the hit efficiency of the present RPC detectors. The “WCS” row corresponds to the scenario in which the efficiencies are listed in Table 3.3. The other rows correspond to the variants of the WCS, in which the efficiency of some stations are setted to 100%. The correspondent results of these variants, are expressed as variations to the WCS [48].



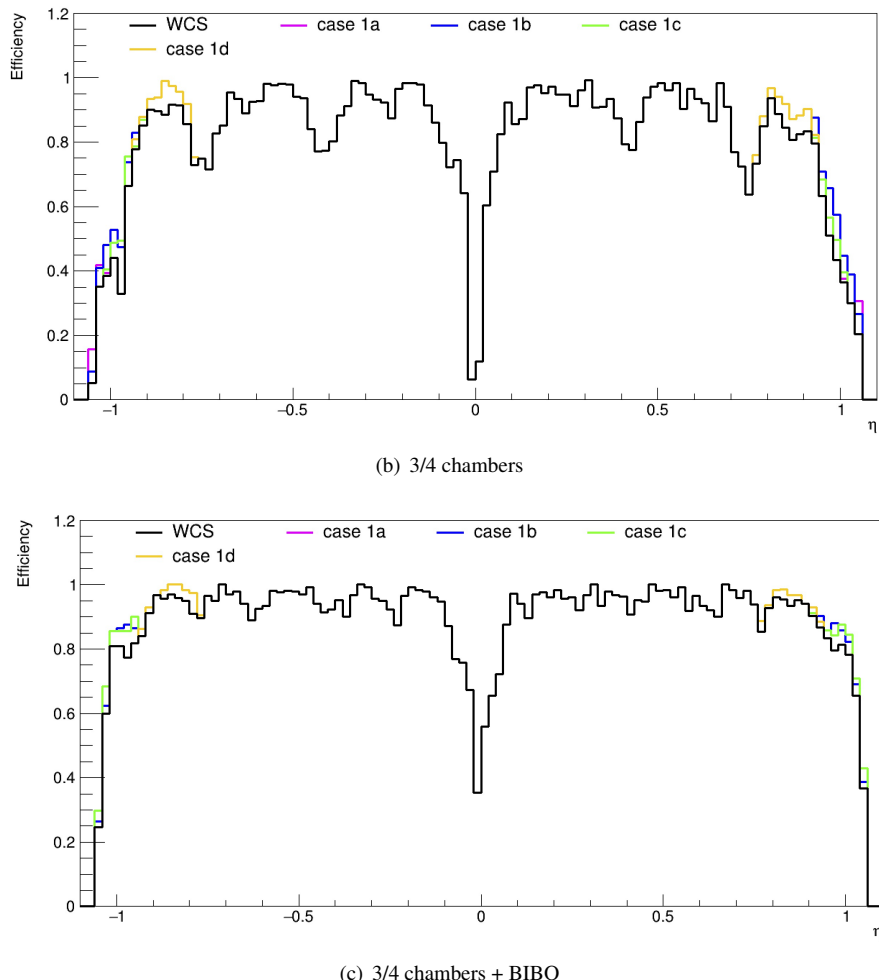


Figure 3.16 – Efficiency times acceptance of the L0 barrel trigger compared to reconstructed muons with $p_T = 50$ GeV as a function of η taking in to account all the variants of the WCS. The histograms show the efficiency of a) the existing 3/3 chambers trigger, of b) the 3/4 chambers trigger including the BI layer, and c) the additional gain from the BI-BO trigger. Efficiency times acceptance is defined as the fraction of reconstructed muons accepted by the trigger, using a simulation that includes the RPC detector efficiency [48].

3.4.2 Dropping BIR and BIM chambers

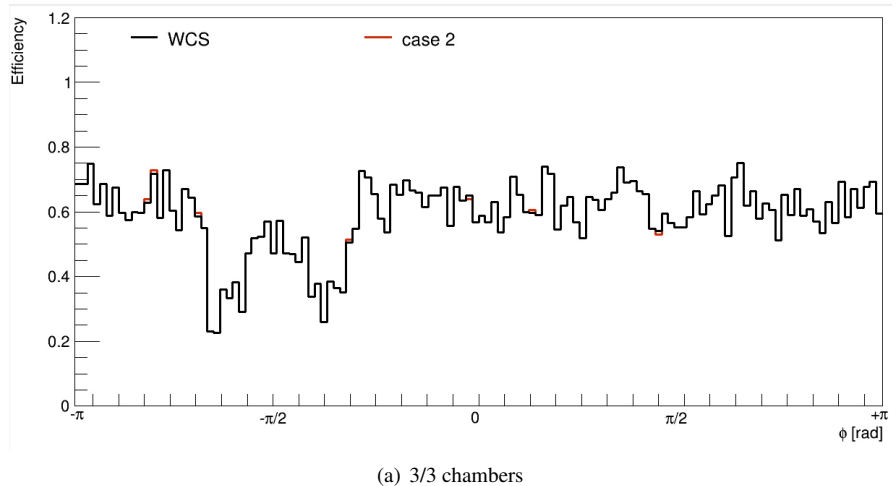
Since the installation of the RPCs in the sectors 11 and 15 (BIM and BIR) seems to be very hard, another special case was performed simulating a scenario in which BI RPC are not installed in these sectors.

The products of muon trigger efficiency and acceptance for the second case are listed in Table 3.6.

The results are also presented in Figure 3.17(c) that compares the "worst-case scenario" with this second case, in which BIM and BIR are turned off. The efficiency distributions show that the absence of BIR and BIM has the most relevant effect on the 3/4 chambers + BIBO logic scheme with a correspondent variation of -3.11%.

BM and BO efficiency (%)	Trigger efficiency x acceptance (%)		
	3/3 chambers	3/4 chambers	3/4 chambers + BIBO
WCS	58.78	83.27	91.89
Case 2 (BIM BIR off)	+0.03	-2.70	-3.11

Table 3.6 – Efficiency times acceptance for the L0 barrel trigger for different assumptions on the hit efficiency of the present RPC detectors. The WCS row corresponds to the scenario in which the efficiencies are listed in Table 3.3. The row "Case 2" corresponds to the case in which RPCs in the sectors 11-15 (BIM and BIR) are turned off. The correspondent results of the Case 2, are expressed as variations to the WCS [48].



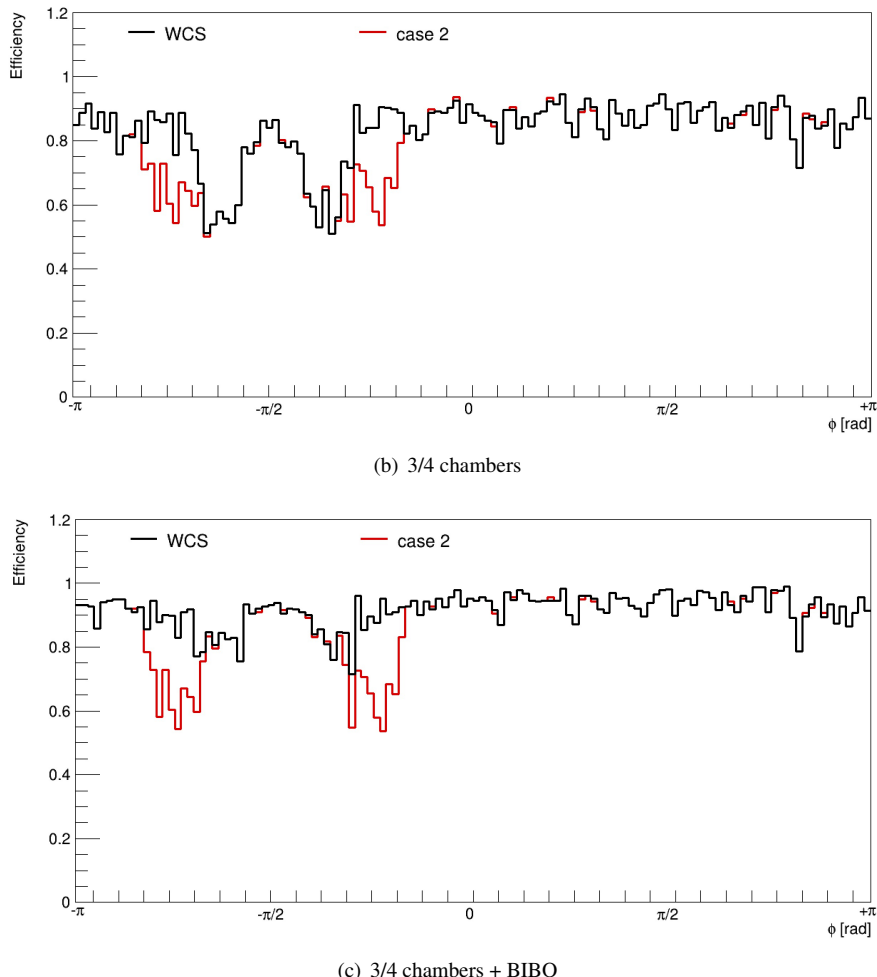


Figure 3.17 – Efficiency times acceptance of the L0 barrel trigger compared to reconstructed muons with $p_T = 50$ GeV as a function of ϕ . The histograms show the efficiency of a) the existing 3/3 chambers trigger, of b) the 3/4 chambers trigger including the BI layer, and c) the additional gain from the BI-BO trigger. Efficiency times acceptance is defined as the fraction of reconstructed muons accepted by the trigger, using a simulation that includes the RPC detector efficiency [48].

CHAPTER 4

Data modeling and object reconstruction

Monte Carlo event generators are the indispensable workhorses of particle physics, bridging the gap between theoretical ideas and first-principles calculations on the one hand, and the complex detector signatures and data of the experimental community on the other hand. In fact, they are mainly used to predict event rates and topologies, simulate possible backgrounds, study detector requirements and study detector imperfections.

The same reconstruction algorithms used to reconstruct data are also applied to all MC samples.

4.1 Event simulation

To understand what the final state of any given physics process will look like, *Monte Carlo simulation* (MC) is used to model both the initial and final state of the process of interest, as well as the propagation of particles through the detector.

A typical MC simulated $p - p$ collision can be schematized as in Figure 4.1. The first step of an event simulation is represented by the extraction of initial-state partons and the evaluation of their momenta using the proton PDFs.

Fixed order matrix element (ME) are used to determine the cross section for the hard scatter integrated over the phase space of the final state particles and it also predicts their momenta.

The particles produced by the hard scatter then undergo a process of *parton showering* (PS), where the quarks and gluons produce a “shower” of further coloured particles.

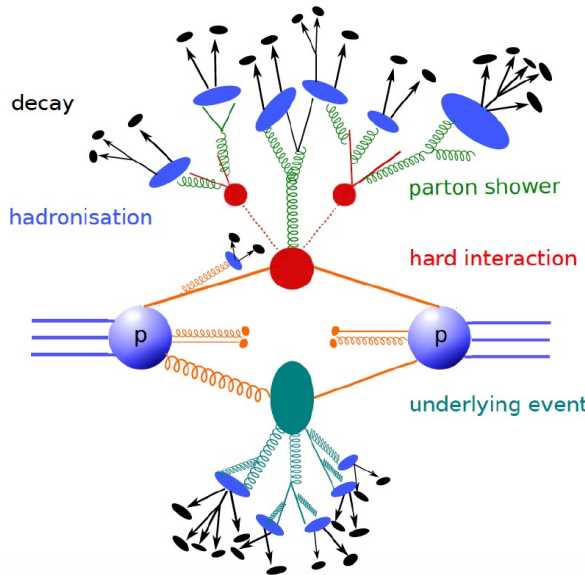


Figure 4.1 – Typical Monte Carlo simulated event with representation of several processes: underlying event, hard scattering, parton shower, hadronisation and decay.

Particles are emitted and produced until the energy scale is below 1 GeV, at which point, the *hadronisation* process starts and colorless hadrons are formed. These hadrons then decay into lighter particles.

As well as the original hard scatter, additional interactions between other partons within the proton must be included in a process known as *underlying event*.

Finally, *pile-up* collisions also overlaid, which originate from collisions of other protons in the beam.

For hadronisation, two main models exist, the string model [49] and the cluster model [50]. In the PYTHIA event generator [51] the string model is used whereas the HERWIG event generator [52] uses the cluster model. The differences in performance of these models can be used to assess the uncertainty due to the model chosen.

The output of the MC event generation process is used as an input to a simulation of the ATLAS detector. This simulation describes all of the detector material and geometry, as well as any defects in the material or electrical problems. The simulation is built using the GEANT4 [53] simulation software.

The output of the detector simulation is reconstructed in the exact same way as data to allow the two to be compared directly.

The simulation of the passage of particles through the detector is very computationally expensive. This is mainly due to simulation of the calorimeters because it is extremely

time consuming to simulate the particle showers. To speed this up, an approximate simulation, ATLASFAST-II (AFII) [54], is often used. This approximate model simulates the particle showers in the calorimeters using parameterised functions applied to particle energy, rather than carrying out the full shower simulation.

4.2 Object reconstruction

This section describes the main reconstruction and identification criteria applied for each physics objects considered in this analysis (electrons, muons, jets, b -tagged jets and missing transverse momentum).

A summary of the object selections is reported in table 4.1.

	p_T	$ \eta $	ID	Isolation	Additional cuts
Electrons	$> 15 \text{ GeV}$	< 2.47	MediumLH	PLVTight	$ d_0^{\text{BL}} \text{ significance} < 5$ $ \Delta z_0^{\text{BL}} \sin \theta < 0.5 \text{ mm}$
Muons	$> 15 \text{ GeV}$	< 2.5	Medium	PLVTight	$ d_0^{\text{BL}} \text{ significance} < 5$ $ \Delta z_0^{\text{BL}} \sin \theta < 0.5 \text{ mm}$
Soft Muons	$> 4 \text{ GeV}$	< 2.5	Tight	–	$ d_0 < 3 \text{ mm}$ $ z_0 \sin \theta < 3 \text{ mm}$ $\Delta R(\mu, \text{jet}) < 0.4$
Jets	$> 25 \text{ GeV}$	< 2.5	PFlow	–	JVT
b -jets	$> 25 \text{ GeV}$	< 2.5	DL1r @ 77 %	–	–

Table 4.1 – Overview of the requirements applied for selecting objects.

4.2.1 Electrons

Electron candidates are reconstructed from energy clusters in the electromagnetic (EM) calorimeter that match a reconstructed track in the inner detector (ID) [55–58]. The clusters are required to be within the range $|\eta| < 2.47$, excluding the transition region between the barrel and endcap calorimeters at $1.37 < |\eta| < 1.52$. Electron candidates must also satisfy a transverse energy requirement of $E_T > 15 \text{ GeV}$.

Further requirements on the electromagnetic shower shape, calorimeter energy to tracker momentum ratio, and other discriminating variables are combined into a likelihood-based object quality cut (LH), optimised for strong background rejection. All electron candidates in this analysis must pass the MediumLH selection.

Electron tracks are also required to be consistent with the beam line applying the requirements: $|d_0^{\text{BL}} \text{ significance}| < 5$ and $|\Delta z_0^{\text{BL}} \sin \theta| < 0.5 \text{ mm}$.

Electrons are further required to be isolated, to reject candidates coming from other

sources than prompt W or Z boson decays (hadrons faking an electron signature, heavy-flavour decays or photon conversions).

The isolation working point used in this analysis is PLVTight.

Correction factors are applied to simulated electrons to take into account the small differences in reconstruction, identification and isolation efficiencies between data and MC simulation.

4.2.2 Muons

Muon candidates are reconstructed by combining a reconstructed track from the ID with one from the muon spectrometer (MS) [59], and are required to have $p_T > 15 \text{ GeV}$ and $|\eta| < 2.5$.

The different combinations of input information (from ID and MS) leads to four different types of reconstructed muons:

- **Combined muons (CB)**: a combined track is formed reconstructing independently tracks in the ID and MS;
- **Segment-tagged muons (ST)**: a track in the ID is classified as a muon if, once extrapolated to the MS, it is associated with at least one local track segment in the MDT or CSC chambers;
- **Calorimeter-tagged muons (CT)**: classification for ID tracks that are matched to an energy deposit in the calorimeter and it is compatible to a minimum ionising particle;
- **Extrapolated muons (ME)**: the reconstructed trajectory of ME muons uses only the MS track and some loose requirement that its origin is the interaction point;

Muons from Z or W boson decays are considered *prompt* muons whereas those coming from pion or kaon decays are *non – prompt* muons.

This analysis needs the suppression of the contribution from non-prompt muons, therefore requirements are placed on muon candidates.

In CB tracks, the variables commonly used in muon identification are:

- **q/p significance**: defined as the absolute value of the difference between the ratio of the charge and momentum of the muons measured in the ID and MS divided by the sum in quadrature of the corresponding uncertainties;
- ρ' : defined as the absolute value of the difference between the transverse momentum measurements in the ID and the MS divided by the p_T of the combined track;
- χ^2 : normalised χ^2 of the combined track fit.

To reject misidentified muon candidates, primarily originating from pion and kaon decays, several quality requirements can be imposed on the muon candidate.

There are four muon identification working points:

- **Tight Muons**: selected to maximise the purity of muons at the cost of some efficiency. Only CB muons with hits in at least two stations of the MS and satisfying the Medium selection criteria are considered. The reconstruction efficiency for Tight muons in the range $20 < p_T < 100$ GeV is 91.8%.
- **Medium Muons**: this is the default working point used by the ATLAS collaboration. Only CB and ME tracks are used. The CB tracks are required to have 3 hits in at least two MDT layers. The reconstruction efficiency for this working point in the range $20 < p_T < 100$ GeV is 96.1%.
- **Loose Muons**: all CB and ME muons that satisfy the Medium requirement are also included in the Loose selection. It is optimised to maximise the reconstruction efficiency, while still retaining only good quality muon tracks. The reconstruction efficiency for Loose muons in the range $20 < p_T < 100$ GeV is 98.1%.
- **High- p_T Muons**: the selection is optimised for analyses searching for high-mass resonances using muons. CB muons are required to pass the Medium selection and have at least three hits in three MS stations. This selection maximises the momentum resolution for muons with $pT > 100$ GeV

The muon candidates in this analysis must pass the Medium identification definition, already described above.

Muon tracks are also required to be consistent with the beam line applying the requirements: $|d_0^{\text{BL}} \text{ significance}| < 3$ and $|\Delta z_0^{\text{BL}} \sin \theta| < 0.5$ mm.

Muons are further required to be isolated and the isolation working point used in this analysis is PLVTight.

Like for electrons, correction factors are applied to simulated muons to account for the small differences between data and simulation.

4.2.3 Soft muons

Different requirements are applied to select and distinguish muons from leptonic decays of the Z and W bosons (referred to as ‘prompt’ or ‘isolated’ muons in the following) and muons from semi-leptonic c-hadron decays (called ‘soft’ or ‘SMT’ muons in the following).

Reconstructed muons with $p_T > 4$ GeV not passing the selection described in the previous section can instead be selected as soft muons.

Soft muons are required to pass the Tight quality requirements [60] and to be closer than 0.4 in ΔR within a selected jet. In case more than one muon passing these criteria is found for a given jet, the soft muon with the lower p_T is chosen. The closest jet to a

soft muon is defined as the ‘SMT’ jet.

Very loose requirements are applied on the impact parameters to remove pathological cases: $|d_0| < 3$ mm and $|z_0 \sin \theta| < 3$ mm.

More details on the soft muon tagging are in Ref. [61].

4.2.4 Jets

Jets are reconstructed using the particle flow algorithm [62].

All jets considered in this analysis should have a transverse momentum $p_T > 25$ GeV and a pseudo-rapidity of $|\eta| < 2.5$.

To suppress jets from in-time pileup, the Jet Vertex Tagger (JVT) discriminant, which is based on a two-dimensional likelihood method, is used [63]. A JVT value of at least 0.59 is required for jets with $p_T < 60$ GeV and $|\eta| < 2.4$, corresponding to an efficiency of 92%.

4.2.5 Jet Flavour Tagging

4.2.5.1 Soft Muon Tagging

4.2.5.2 Recurrent Deep-Learning DL1r

4.2.6 Missing transverse momentum

The missing transverse momentum, E_T^{miss} , is a measure of the momentum imbalance, usually due to escaping neutrinos. It is calculated as the magnitude of the negative vector sum of the momenta in the transverse plane of all selected calibrated physics objects in the event [64, 65].

To account for the soft hadronic activity, a soft term built from tracks that are associated to the hard-scatter vertex but are not associated to any of the reconstructed objects. The soft term is included in order to account for low-momentum particles that are not identified among the final state objects [66–68].

It also includes an extra term to account energy losses due to the detector inefficiencies and resolution leading to the mis-measurement of the true transverse energy of the final interacting objects.

4.2.7 Overlap removal

In order to avoid double counting of single final state objects, like e.g. an isolated electron being reconstructed both as an electron and as a jet with the requirements above, a procedure is followed to remove overlaps between final state objects. This is the sequence of operation that are performed to solve these ambiguities, as implemented as the harmonized option [69] in the `AssociationUtils` [70] package:

- Electron candidates which share a track with a muon candidate are removed.
- If the distance in ΔR between a jet and an electron candidate is $\Delta R < 0.2$, then the jet is dropped. If multiple jets are found with this requirement, only the closest one is dropped.
- If the distance in ΔR between a jet and a baseline electron is $0.4 < \Delta R < 0.2$, then the electron is dropped.
- If the distance in ΔR between a jet and a muon candidate is $\Delta R < 0.4$, then: if the jet has more than 2 associated tracks then the muon is dropped, otherwise the jet is removed.

No overlap removal is performed on muons used for the Soft Muon Tagging.

CHAPTER 5

Search for the FCNC decay of top-quark in c-quark and Z boson

This chapter presents a search for the Flavor-Changing-Neutral-Current decay of top-quark in c-quark and Z boson, denoted FCNC tZc . The study uses a data sample of proton-proton collisions at $\sqrt{s} = 13$ TeV recorded in full Run2 (since 2015 to 2018) by the ATLAS experiment, and targets final states with three leptons (either electrons or muons). I took in charge most of the analysis, from the event selection up to the final results. In particular, an important fraction of my work was dedicated to the event selection using the SMT technique and the design and optimization of the multivariate analysis.

5.1 Physics motivation

The heaviest particle in the Standard Model (SM), the top quark, decays almost exclusively to a W -boson and a bottom quark [71]. In proton-proton (pp) collisions, top quarks are produced dominantly in pairs, via the strong interaction, but also singly, via the electroweak interaction.

Within the SM, flavour changing neutral currents (FCNC) processes are forbidden at tree level due to the Glashow-Iliopoulos-Maiani mechanism [5] and the approximate diagonality of the Cabibbo-Kobayashi-Maskawa matrix [71] causes the suppression of such processes at higher orders. Nonetheless, there are several scenarios beyond the Standard Model (BSM) that can significantly enhance the FCNC processes in the top quark sector, opening a door for its detection at the Large Hadron Collider (LHC) [6, 21–24, 29].

The analysis presented in the following searches for FCNC tZc processes. A comparison between SM and BSM models predictions for the branching ratios of top quark decays to an up or a charm quark and a Z boson is shown in Table 5.1.

Table 5.1 – The theoretical values for the branching ratios of FCNC top decays predicted by the SM, the quark singlet model (QS) [6], the minimal supersymmetric standard model (MSSM) [22], SUSY with R parity violation (RPV SUSY) [23] and warped extra dimensions (RS) (without prediction to up quark interactions) [24] models.

Process	SM	QS	MSSM	RPV SUSY	RS
$t \rightarrow Zu$	10^{-17}	$\leq 10^{-4}$	$\leq 10^{-7}$	$\leq 10^{-6}$	–
$t \rightarrow Zc$	10^{-14}	$\leq 10^{-4}$	$\leq 10^{-7}$	$\leq 10^{-6}$	$\leq 10^{-5}$

The search for FCNC tZc processes can be performed by analysing the top quark decays in $t\bar{t}$ events as well as the production of single-top quarks (see Figure 5.1). In the former channel, one of the top quarks decays through FCNC and the other through the dominant mode ($t \rightarrow Wb$). The latter channel is characterised by a final state composed of a single top quark and a Z boson. The main difference between the final state of decay and production modes is the presence of one additional jet.

The analysis presented in the following targets both production and decay mode. This search is done using pp collision data collected by the ATLAS detector at a centre-of-mass energy of 13 TeV and corresponding to an integrated luminosity of 139 fb^{-1} . The analysis targets both events with the production of a Z boson and a single-top quark decaying to a W boson and a b-quark and events with the production of top quark pairs, where one top quark decays to a Z boson and a light quark (up or charm) and the other top quark decays to a W boson and a b-quark. For both modes, the Z boson decays into two charged leptons (electrons or muons including those coming from leptonic τ -lepton decays) and the W boson from the top quark decays leptonically too.

In a model independent way, the anomalous couplings can be described by the so called effective field theory (EFT). This theory considers an extension of the SM Lagrangian \mathcal{L}_{SM} by operators in higher-dimensions of the mass suppressed by the scale of new physics Λ as shown in eq. (5.1). Dimension-5 operators are not considered in this analysis due to the introduction of lepton-flavour violating processes. Therefore, the anomalous couplings can be approximated with dimension-6 operators $O_i^{(6)}$ whose strength is given by the Wilson coefficients $C_i^{(6)}$.

$$\mathcal{L} = \mathcal{L}_{SM} + \frac{1}{\Lambda^2} \sum_i C_i^{(6)} O_i^{(6)} \quad (5.1)$$

Experimental limits on the branching ratio of FCNC tZc decays were previously es-

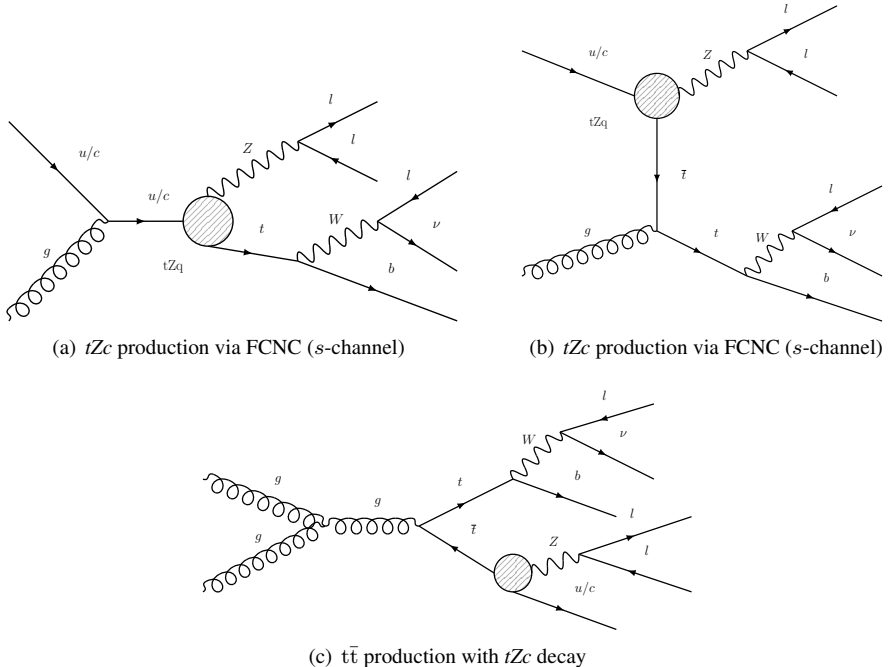


Figure 5.1 – Examples of lowest order Feynman diagrams for tZc production via FCNC in (a) the s -channel and (b) the t -channel. Example of the lowest order Feynman diagrams for (c) $t\bar{t}$ production, with one top-quark decaying through the SM and the other via tZc . The vertex labelled as tZq corresponds to the coupling responsible for the FCNC interaction.

Established by experiments at the Large Electron-Positron Collider (LEP) [72–75], the Hadron-Electron Ring Accelerator (HERA) [76], the Tevatron [10, 77] and the Large Hadron Collider (LHC) [78–80]. The ATLAS and the CMS collaborations obtained limits at the 95 % confidence level (CL) for these processes using data collected at $\sqrt{s}=13$ TeV and $\sqrt{s}=8$ TeV, focusing on FCNC top-quark decays [78, 79], or both production and decay modes combined [80]. A summary of the ATLAS and CMS results on the limits on FCNC couplings is shown in fig. 5.2. The actual observed limits on the FCNC tZc couplings from ATLAS is $BR(t \rightarrow cZ) < 2.4 \times 10^{-4}$ [78]. Recent studies were done on the interference effects on the tZc and $t\gamma q$ anomalous couplings, concluding that these effects are smaller than the variations of the systematics uncertainties considered [81]. Therefore, both decay and production modes are taken into account in this analysis to improve the results on the limits for tZc anomalous couplings.

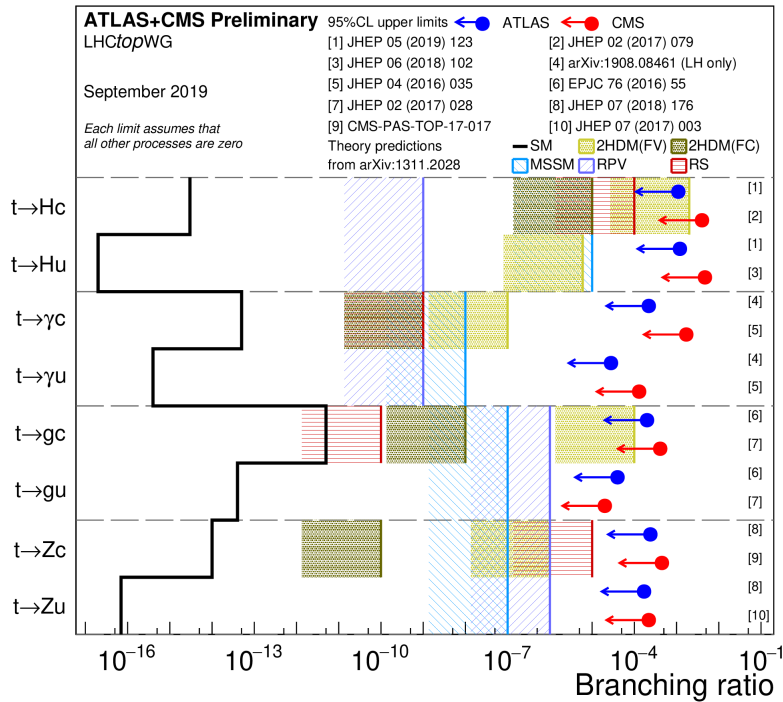


Figure 5.2 – Summary of the current 95% confidence level observed limits on the branching ratios of the top quark decays via flavour changing neutral currents to a quark and a neutral boson $t \rightarrow Xq$ ($X = g, Z, \gamma$, or H ; $q = u$ or c) by the ATLAS and CMS Collaborations compared to several new physics models. The ATLAS limits on $t \rightarrow q$ are valid for the case of a purely left-handed coupling. Status of figure: September 2019 (Top2019)

5.2 Analysis strategy

5.3 Data and Monte Carlo samples

5.4 Event selections and reconstruction

$$\chi^2 = \frac{(m_{j_{SM} l_a l_b}^{reco} - m_{t_{FCNC}})^2}{\sigma_{t_{FCNC}}^2} + \frac{(m_{j_{bjet} l_c \nu}^{reco} - m_{t_{SM}})^2}{\sigma_{t_{SM}}^2} + \frac{(m_{l_c \nu}^{reco} - m_W)^2}{\sigma_W^2} \quad (5.2)$$

5.4.1 Top quarks reconstruction

5.4.2 Signal Region definition

5.5 Background estimation

5.5.1 Control Regions definitions

5.5.2 Fake composition

5.6 Separation of signal from background events

5.6.1 GBDT discriminant definition

5.6.2 Input variables

5.6.3 GBDT training and evaluation

5.6.4 GBDT performance and over-training checks

5.7 Systematic uncertainties

5.7.1 Sources of systematic uncertainties

5.7.2 Acceptance and shape uncertainties

5.8 Additional Signal Regions and alternative c-tagger

CHAPTER 6

Statistical analysis for tZc coupling

6.1 Strategy

6.2 Results

6.2.1 Background-only fit in CRs

6.2.2 Signal+Background fit in SR3

6.2.3 Signal+Background fit in SRs+CRs

CHAPTER 7

Conclusions

APPENDIX A

Mass Resolution

References

- [1] E. Fermi, *Il Nuovo Cimento* (1934) **11**, 1 (2008).
- [2] F. L. Wilson, *Am.J.Phys* **36**, 1150 (1968).
- [3] C. S. Wu, E. Ambler, R. W. Hayward, D. D. Hoppes, and R. P. Hudson, *Phys. Rev.* **105**, 1413 (1957).
- [4] P. Renton, *Electroweak Interactions: An Introduction to the Physics of Quarks and Leptons* (1990).
- [5] S. L. Glashow, J. Iliopoulos, and L. Maiani, *Phys. Rev. D* **2**, 1285 (1970).
- [6] J. Aguilar-Saavedra, “Top flavour-changing neutral interactions: theoretical expectations and experimental detection,” (2004), arXiv:hep-ph/0409342 [hep-ph].
- [7] N. Cabibbo, *Meeting of the Italian School of Physics and Weak Interactions Bologna, Italy, April 26-28, 1984*, *Phys. Rev. Lett.* **10**, 531 (1963).
- [8] M. Kobayashi and T. Maskawa, *Progress of Theoretical Physics* **49**, 652 (1973).
- [9] Z. Ligeti, *Int. J. Mod. Phys. A* **20**, 5105 (2005), arXiv:hep-ph/0408267 [hep-ph].
- [10] F. Abe *et al.* (CDF Collaboration), *Phys. Rev. Lett.* **74**, 2626 (1995).
- [11] S. Abachi *et al.* (D0 Collaboration), *Phys. Rev. Lett.* **74**, 2632 (1995).
- [12] R. Aaij *et al.* (LHCb Collaboration), *Phys. Rev. Lett.* **115**, 112001 (2015).
- [13] M. Tanabashi *et al.* (Particle Data Group), *Phys. Rev. D* **98**, 030001 (2018).
- [14] W. Bernreuther, *J. Phys. G* **35**, 083001 (2008), arXiv:0805.1333 [hep-ph].
- [15] D0 Collaboration website, “[Useful Diagrams of Top Signals and Backgrounds](#),” .
- [16] G. Aad *et al.* (ATLAS), *Phys. Lett. B* **716**, 1 (2012), arXiv:1207.7214 [hep-ex].
- [17] F. Zwicky, *General Relativity and Gravitation* **41**, 207 (2009).

- [18] N. Aghanim *et al.* (Planck), (2018), arXiv:1807.06209 [astro-ph.CO].
- [19] J. A. Aguilar-Saavedra, Acta Phys. Polon. **B35**, 2695 (2004), arXiv:hep-ph/0409342 [hep-ph].
- [20] J. A. Aguilar-Saavedra, Phys. Rev. **D67**, 035003 (2003), arXiv:hep-ph/0210112 [hep-ph].
- [21] D. Atwood, L. Reina, and A. Soni, Phys. Rev. D **55**, 3156 (1997).
- [22] J. J. Cao, G. Eilam, M. Frank, K. Hikasa, G. L. Liu, I. Turan, and J. M. Yang, Phys. Rev. D **75**, 075021 (2007).
- [23] J. M. Yang, B.-L. Young, and X. Zhang, Phys. Rev. D **58**, 055001 (1998).
- [24] K. Agashe, G. Perez, and A. Soni, Phys. Rev. D **75**, 015002 (2007).
- [25] P. Hung, Y.-X. Lin, C. S. Nugroho, and T.-C. Yuan, Nuclear Physics B **927**, 166 (2018).
- [26] K. Agashe *et al.* (Top Quark Working Group) (2013) arXiv:1311.2028 [hep-ph].
- [27] S. L. Glashow and S. Weinberg, Phys. Rev. D **15**, 1958 (1977).
- [28] E. A. Paschos, Phys. Rev. D **15**, 1966 (1977).
- [29] V. D. Barger, M. S. Berger, and R. J. N. Phillips, Phys. Rev. **D52**, 1663 (1995), arXiv:hep-ph/9503204 [hep-ph].
- [30] Z. Maki, M. Nakagawa, and S. Sakata, Prog. Theor. Phys. **28**, 870 (1962).
- [31] G. C. Branco, P. M. Ferreira, L. Lavoura, M. N. Rebelo, M. Sher, and J. P. Silva, Phys. Rept. **516**, 1 (2012), arXiv:1106.0034 [hep-ph].
- [32] G. Couture, C. Hamzaoui, and H. König, Phys. Rev. D **52**, 1713 (1995).
- [33] L. Evans and P. Bryant, Journal of Instrumentation **3**, S08001 (2008).
- [34] E. Mobs, “The CERN accelerator complex - August 2018. Complexe des accélérateurs du CERN,” .
- [35] “LHC public plots,” ATLAS Twiki.
- [36] G. Aad *et al.* (ATLAS), JINST **3**, S08003 (2008).
- [37] The ATLAS collaboration, *ATLAS magnet system: Technical Design Report* (1997).
- [38] The ATLAS collaboration, *ATLAS liquid argon calorimeter: Technical Design Report* (1996).
- [39] The ATLAS collaboration, *ATLAS muon spectrometer : Technical Design Report* (1997).
- [40] The ATLAS collaboration, *ATLAS high-level trigger, data acquisition and controls: Technical Design Report* (2003).
- [41] “LHC upgrades and operation,” CERN Website.
- [42] *Technical Design Report for the Phase-II Upgrade of the ATLAS Muon Spectrometer*, Tech. Rep. CERN-LHCC-2017-017. ATLAS-TDR-026 (CERN, Geneva, 2017).
- [43] T. Kawamoto, S. Vlachos, L. Pontecorvo, J. Dubbert, G. Mikenberg, P. Iengo, C. Dallapiccola, C. Amelung, L. Levinson, R. Richter, and D. Lellouch, *New Small Wheel Technical Design Report*, Tech. Rep. CERN-LHCC-2013-006. ATLAS-TDR-020 (2013) aTLAS New Small Wheel Technical Design Report.

- [44] G. Aielli, C. Amelung, D. Boscherini, R. Cardarelli, M. Corradi, L. Han, V. Izzo, O. Kortner, H. Kroha, D. Levin, L. Massa, L. Paolozzi, R. Santonico, and R. Vari (ATLAS Collaboration), *The ATLAS BIS78 Project*, Tech. Rep. ATL-MUON-INT-2016-002 (CERN, Geneva, 2016).
- [45] ATLAS Collaboration (ATLAS), *muTrigNt_write code*, Tech. Rep.
- [46] ATLAS Collaboration (ATLAS), *Muon Upgrade Studies Twiki*, Tech. Rep.
- [47] L.Marcoccia, *Phase II Upgrade : High-eta tagger + RPC (Muon Week)*, Tech. Rep. (2018).
- [48] L. Marcoccia, *Efficiency studies on emulated RPC for the Phase-II Upgrade of the ATLAS Muon Spectrometer*, Tech. Rep. ATL-COM-MUON-2019-060 (CERN, Geneva, 2019).
- [49] B. Andersson, G. Gustafson, G. Ingelman, and T. Sjöstrand, *Physics Reports* **97**, 31 (1983).
- [50] G. Marchesini and B. Webber, *Nuclear Physics B* **238**, 1 (1984).
- [51] T. Sjöstrand, S. Mrenna, and P. Skands, *Journal of High Energy Physics* **2006**, 026 (2006).
- [52] M. Bähr, S. Gieseke, M. A. Gigg, D. Grellscheid, K. Hamilton, O. Latunde-Dada, S. Plätzer, P. Richardson, M. H. Seymour, A. Sherstnev, and B. R. Webber, *The European Physical Journal C* **58**, 639 (2008).
- [53] S. Agostinelli *et al.* (GEANT4), *Nucl. Instrum. Meth. A* **506**, 250 (2003).
- [54] E. Richter-Was, D. Froidevaux, and L. Poggiali, *ATLFAST 2.0 a fast simulation package for ATLAS*, Tech. Rep. ATL-PHYS-98-131 (CERN, Geneva, 1998).
- [55] ATLAS Collaboration, “Electron identification measurements in ATLAS using $\sqrt{s} = 13$ TeV data with 50 ns bunch spacing,” ATL-PHYS-PUB-2015-041 (2015).
- [56] ATLAS Collaboration, “Electron and photon energy calibration with the ATLAS detector using data collected in 2015 at $\sqrt{s} = 13$ TeV,” ATL-PHYS-PUB-2016-015 (2016).
- [57] ATLAS Collaboration, “Electron efficiency measurements with the ATLAS detector using the 2015 LHC proton–proton collision data,” ATLAS-CONF-2016-024 (2016).
- [58] ATLAS Collaboration, *Eur. Phys. J. C* **79**, 639 (2019), arXiv:1902.04655 [hep-ex].
- [59] ATLAS Collaboration, *Eur. Phys. J. C* **76**, 292 (2016), arXiv:1603.05598 [hep-ex].
- [60] *Muon Combined Performance in Run 2 (25 ns runs)*, Tech. Rep. ATL-COM-MUON-2015-093 (Geneva, 2015).
- [61] *Calibration of the Soft Muon Tagger in Run-2 data*, Tech. Rep. ATL-COM-PHYS-2017-1110 (CERN, Geneva, 2017) updates to be expected.
- [62] ATLAS Collaboration, *Eur. Phys. J. C* **77**, 466 (2017), arXiv:1703.10485 [hep-ex].
- [63] ATLAS Collaboration, “Tagging and suppression of pileup jets with the ATLAS detector,” ATLAS-CONF-2014-018 (2014).
- [64] G. Aad *et al.* (ATLAS), *Eur. Phys. J. C* **77**, 241 (2017), arXiv:1609.09324 [hep-ex].
- [65] A. Collaboration, *The European Physical Journal C* **77**, 241 (2017).
- [66] ATLAS Collaboration, *Eur. Phys. J. C* **72**, 1844 (2012), arXiv:1108.5602 [hep-ex].
- [67] ATLAS Collaboration, *Eur. Phys. J. C* **77**, 241 (2017), arXiv:1609.09324 [hep-ex].

- [68] ATLAS Collaboration, “Performance of missing transverse momentum reconstruction with the ATLAS detector in the first proton–proton collisions at $\sqrt{s} = 13$ TeV,” ATL-PHYS-PUB-2015-027 (2015).
- [69] D. Adams *et al.*, *Recommendations of the Physics Objects and Analysis Harmonisation Study Groups 2014*, Tech. Rep. ATL-PHYS-INT-2014-018 (CERN, Geneva, 2014).
- [70] <https://svnweb.cern.ch/trac/atlasoff/browser/PhysicsAnalysis/AnalysisCommon/AssociationUtils/trunk/doc/REA> accessed: 2019-09-09.
- [71] C. Patrignani *et al.* (ParticleDataGroup), *Phys. Rev. D* **98**, 030001, 1898 p (2018).
- [72] A. Heister *et al.* (ALEPH), *Phys. Lett. B* **543**, 173 (2002), arXiv:hep-ex/0206070 [hep-ex].
- [73] J. Abdallah *et al.* (DELPHI), *Phys. Lett. B* **590**, 21 (2004), arXiv:hep-ex/0404014 [hep-ex].
- [74] G. Abbiendi *et al.* (OPAL), *Phys. Lett. B* **521**, 181 (2001), arXiv:hep-ex/0110009 [hep-ex].
- [75] P. Achard *et al.* (L3), *Phys. Lett. B* **549**, 290 (2002), arXiv:hep-ex/0210041 [hep-ex].
- [76] H. Abramowicz *et al.* (ZEUS), *Phys. Lett. B* **708**, 27 (2012), arXiv:1111.3901 [hep-ex].
- [77] D0 Collaboration (D0), *Phys. Lett. B* **701**, 313 (2011), arXiv:1103.4574 [hep-ex].
- [78] ATLAS Collaboration, *JHEP* **07**, 176 (2018), arXiv:1803.09923 [hep-ex].
- [79] CMS Collaboration (CMS), *Phys. Rev. Lett.* **112**, 171802 (2014), arXiv:1312.4194 [hep-ex].
- [80] CMS Collaboration, *JHEP* **07**, 003 (2017), arXiv:1702.01404 [hep-ex].
- [81] M. Barros *et al.*, *Eur. Phys. J. Plus* **135**, 339 (2020).